Theses and Dissertations

Summer 2010

Real gas effects in heated gas inflators

Matthew John Zanker

University of Iowa

Recommended Citation

Zanker, Matthew John. "Real gas effects in heated gas inflators." MS (Master of Science) thesis, University of Iowa, 2010.
http://ir.uiowa.edu/etd/768.

REAL GAS EFFECTS IN HEATED GAS INFLATORS

by

Matthew John Zanker

A thesis submitted in partial fulfillment
of the requirements for the
Master of Science degree in Mechanical Engineering
in the Graduate College of
The University of Iowa

July 2010

Thesis Supervisor: Professor P. Barry Butler

Graduate College
The University of Iowa
Iowa City, Iowa

CERTIFICATE OF APPROVAL

_____

MASTER'S THESIS

_____

This is to certify that the Master's thesis of

Matthew John Zanker

has been approved by the Examining Committee
for the thesis requirement for the Master of Science
degree in Mechanical Engineering at the July 2010 graduation.

Thesis Committee: _____
                              P. Barry Butler, Thesis Supervisor

                              _____
                              Ching-Long Lin

                              _____
                              Albert Ratner

ABSTRACT

Currently, almost all new vehicles are equipped with airbags. A common type of airbag inflator is the Heated Gas Inflator (HGI). These inflators are cylindrical shaped canisters that are filled to very high pressures with a gaseous mixture of fuel and air. The mixture is ignited from one or both ends of the cylinder. The resulting high temperatures from combustion heat the excess air, which is then used to inflate the airbag. Once the mixture is ignited large pressure waves form, traveling along the length of the tube. These waves, inherent to the design of the inflator, do not allow the use of a volume averaged assumption for the combustion chamber. Therefore, it is necessary to use a Computational Fluid Dynamics (CFD) code to model the dynamic nature of the inflator. Commercial CFD codes are readily available that could be used to model the HGI. These codes use the Ideal Gas Law to calculate the properties of the mixture. The high pressures in an HGI do allow for the use of an ideal gas assumption. Instead, a Real Gas equation of state must be used.

An existing Airbag Inflator Model that was capable of Real Gas equation of state calculations had been previously created to simulate solid propellant inflators. In order to properly model the wave dynamics in an HGI and include Real Gas calculations, a CFD model has been added to the Airbag Inflator Model. The CFD model must be capable of handling multiple species of gases and be able to properly model the sharp gradients associated with large pressure waves and changes in chemical species. Therefore, a high-resolution shock capturing technique is used to handle the homogeneous part of the governing equations. The non-homogeneous terms of the governing equations are solved using an ordinary differential equations solver. In order to combine the solutions, a time

splitting technique is used to combine the solutions from the homogeneous and non-homogeneous parts of the governing equations.

The addition of the CFD model to an Airbag Inflator Model with Real Gas equation of state capabilities provides a very useful tool in the design of HGIs. The model can be used to ensure that a design does not produce unexpected large magnitude pressure waves that could possibly cause dangerous mechanical failures. Later models of HGIs have ignitors at each end of the cylinder. The secondary ignitor can be delayed to vary the production rate of the exhaust gasses, depending on the severity of the crash. This time delay is an additional parameter that can have an effect on the wave dynamics in the HGI. The addition of the CFD model to the Airbag Inflator Model provides a fast and economical way to predict the outcome of any change in the design parameters of an HGI.

TABLE OF CONTENTS

LIST OF TABLES

LIST OF FIGURES

LIST OF NOMENCLATURE

Variables, Greek Letters, and Symbol Definitions

A_i — Pre-exponential factor in the rate constant for the ith reaction

A_{flow} — Area of outflow nozzle (cm^2)

a — Intermolecular attractive term in the cubic equations of state ($dyne \cdot cm^4/mole^2$)

a — Speed of sound

a_m — Mixture 'a' ($dyne \cdot cm^4/mole^2$), see Eq. (2.28)

a_{nk} — Coefficients to fits of thermodynamic data

A^* — Dimensionless form of 'a' for mixture, see Eq. (2.26)

b — Volume correction term in cubic equations of state ($cm^3/mole$)

b_m — Mixture 'b' ($cm^3/mole$), see Eq. 2.29

B^* — Dimensionless form of 'b' for mixture, see Eq. (2.27)

C_{pk}° — Standard-state species specific heat at constant pressure ($ergs/mole \cdot K$)

c — Speed of sound (cm/s)

E — Total energy per unit volume ($ergs/cm^3$)

E_i — Activation energy for the ith reaction ($cal/mole$)

e — Specific internal energy ($ergs/g$) (thermal only)

F — Flux vector in the axial direction

F^+ — Positive flux

F^- — Negative flux

G — Flux vector in the radial direction

H_k° — Standard-state enthalpy of the k_{th} species ($ergs/mole$)

H	Mixture molar enthalpy (ergs/mole)
h_o	Specific enthalpy of mass flow out of the continuum (erg/g)
h_{nozzle}	Enthalpy for nozzle condition (ergs/g)
k_{fi}	Forward reaction rate for the ith reaction
M	Mach number
$\dot{m}_o$	Mass flow rate out of the continuum (g/s·cm^3)
m	Mass (g)
P	Absolute pressure (dyne/cm^2)
P_{cr}	Critical pressure ratio
P_c	Critical pressure (dyne/cm^2)
R	Universal gas constant (ergs/mole·K)
R_c	Universal gas constant, same units as E_i (cal/mole·K)
S	Source term vector
T	Temperature (K)
T_c	Critical temperature (K)
T_{o1}	Stagnation temperature of cell with outflow nozzle (K)
T_1	Temperature of cell with outflow nozzle (K)
T_{nozzle}	Temperature of gas at the nozzle (K)
t	Time (seconds)
u	Constant in the cubic equations of state, see Table 2.1
U	Vector of conserved variables
U	Mixture molar internal energy (ergs/mole)
V	Volume (cm^3)

V	Velocity Vector
V_x	Velocity in the x direction (cm/s)
V_y	Velocity in the y direction (cm/s)
w	Constant in the cubic equations of state, see Table 2.1
x	Displacement on x-axis in a Cartesian or cylindrical system (cm)
Y_k	Mass fraction of species k
y	Displacement on y-axis in a Cartesian system (cm)
Z	Compressibility factor
λ	Eigenvalue
η	Flux limiter parameter
ϖ	Flux limiter parameter
ρ	Density (g/cm^3)
β_i	Temperature exponent for the i_{th} reaction
γ	Specific heat ratio
ρ_{nozzle}	Density at the nozzle (g/cm^3)

Abbreviations

atm	Atmosphere
cc	cubic centimeters
CFD	Computational Fluid Dynamics
CFL	Courant-Friedrichs-Levy
CJ	Chapman-Jouguet
EOS	Equation of state
HGI	Heated gas Inflators

LSODE	Livermore Solver for Ordinary Differential Equations
ms	Millisecond
mm	Millimeters
ODE	Ordinary Differential Equation
PDE	Partial Differential Equation
psi	Pounds per square inch
TVD	Total variation diminishing

CHAPTER 1

INTRODUCTION

1.1 Background

All new vehicles sold in the United States are equipped, at a minimum, with both

driver- and passenger-side airbags. Airbags are part of a comprehensive vehicle safety

system that can include such features as: anti-lock and smart braking systems, crash

detection sensors, active occupant restraint devices, whiplash protection, driver sleep

detection, roll-over prevention, and pedestrian impact protection. All components of the

vehicle's safety system must conform to performance and reliability standards mandated

by the Federal government. With respect to airbag systems, this includes tight

performance specifications over a wide range of ambient operating conditions (-30 C

through +65 C) for the primary bag inflation parameters, i.e., rate of inflation and peak

airbag pressure. In addition, the chemical composition of the inflator effluent gas is

controlled by Federal emission standards since it eventually is vented from the airbag into

the cabin air.

1.2 Airbag Inflator

At the core of an airbag occupant system is the so-called "inflator," or "gas

generator." The inflator is a device designed to deliver gas to the airbag at a specified

flow rate, composition and temperature. Over the years, a number of different inflator

designs have been developed that satisfy the performance requirements. While the

different inflator designs serve the same general purpose (i.e., rapidly produce gas to

inflate an airbag), the method used to generate and deliver the gas varies. Most vehicles

in service today have airbag inflators that can be categorized based on their gas-

generation method as one of the following: i) pyrotechnic inflator, ii) hybrid pyrotechnic inflator, and iii) combustible gas inflators, also referred to as a heated gas inflator (HGI).

1.3 Pyrotechnic Inflators

In the first commercially viable airbag systems, the inflator relied entirely on the combustion of solid propellant for gas generation. Figure 1.1 presents a cutaway view of a typical passenger-side pyrotechnic inflator. The equivalent driver-side pyrotechnic inflator would have the same basic elements but would be disk shaped rather than cylindrical in order to conform to the steering column installation requirements. In a pyrotechnic inflator, the propellant (Item A, Fig. 1.1) is packed at high solids-loading in a thick-walled combustion chamber (Item D, Fig. 1.1). The propellant and igniter (Item B, Fig. 1.1) are sealed from the external environment by a hermetically sealed rupture film (Item C, Fig. 1.1). The rupture film acts to keep the propellant dry throughout its expected 20-30 year lifetime. It also serves to confine the propellant product gases for the first few milliseconds following ignition, resulting in rapid pressurization and fast flame spread throughout the propellant bed. Surrounding the propellant is a multi-layered mesh screen (Item E, Fig. 1.1). Discharge orifices (Item F, Fig. 1.1) pass though the exterior wall of the vessel allowing the plenum gas to discharge into the adjacent airbag.
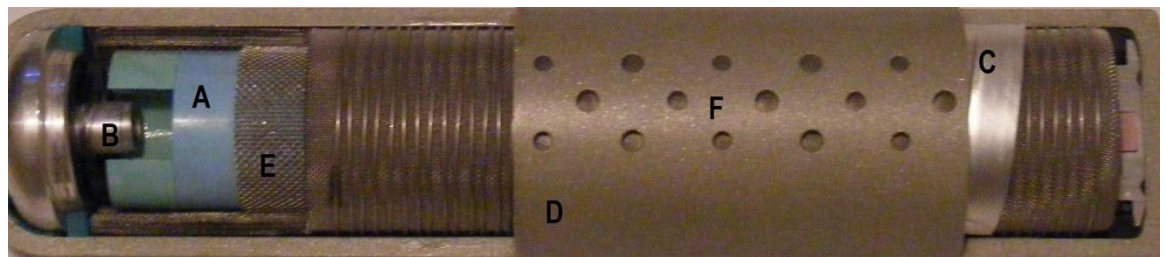
Figure 1.1 Cutaway view of a passenger-side pyrotechnic inflator.

The most common propellant used in the earliest pyrotechnic inflators was sodium azide (NaN_3) mixed with metal-oxides (e.g., CuO or Fe_2O_3), flame accelerants (e.g., $NaNO_3$) and small amounts of inert binders (e.g., SiO_2). The mixture of fuel, oxidizer and binder is consolidated into milligram-sized "grains" or larger tablets using a mechanical press. The grains shown in Fig. 1.1 are large, multi-perforated disks. Azide-based propellants were initially selected because of their relatively low combustion temperature and high yield of nitrogen in the product mixture. However, azide-based propellants produce a significant amount of condensed-phase products of combustion (Berger and Butler, 1995). For example, a typical mixture of sodium azide and iron oxide produces gaseous nitrogen and condensed-phase slag ($Na_2O(s)$, $Fe(s)$, $FeO(s)$) on approximately a 1:1 mass ratio at an adiabatic flame temperature of approximately 1,300 K. The high percentage of slag requires the filter screen (Item E, Fig. 1.1) to remove it from the gaseous products.

A typical sequence of events for a pyrotechnic inflator is as follows: (Butler et al., 1993) upon detection of impact by the vehicle's collision sensors, an electrical signal initiates a small, high-energy pyrotechnic igniter located inside the combustion chamber. While the exact composition of the igniter varies depending on the manufacturer, it typically generates a very hot gas mixed with molten metallic particles. Heat flux from the igniter's products of combustion to the propellant surface results in ignition. To promote a rapid ignition sequence of all propellant grains, the propellant surface is often coated with a flame accelerant. Ignition spreads across the surface of all propellant grains and, within a few milliseconds, the combustion chamber pressure reaches the burst pressure of the rupture film, resulting in discharge of the products from the combustion

chamber. As the high-pressure products leave the combustion chamber they follow a

tortuous path through a filter mechanism which acts to cool the gas and capture the

molten and solid products of combustion. In most designs, the filter is made of a multi-

layered steel mesh to introduce high surface area for heat transfer and small passages to

capture the solid residue. Figure 1.2 illustrates typical pressure-time profiles for the

combustion chamber (Fig. 1.2, Part a) and a standard discharge test tank (Fig. 1.2, Part b).

Key inflator performance parameters are shown on the figures. It should be noted that the

inflator pressure is spatially uniform throughout the combustion chamber because the
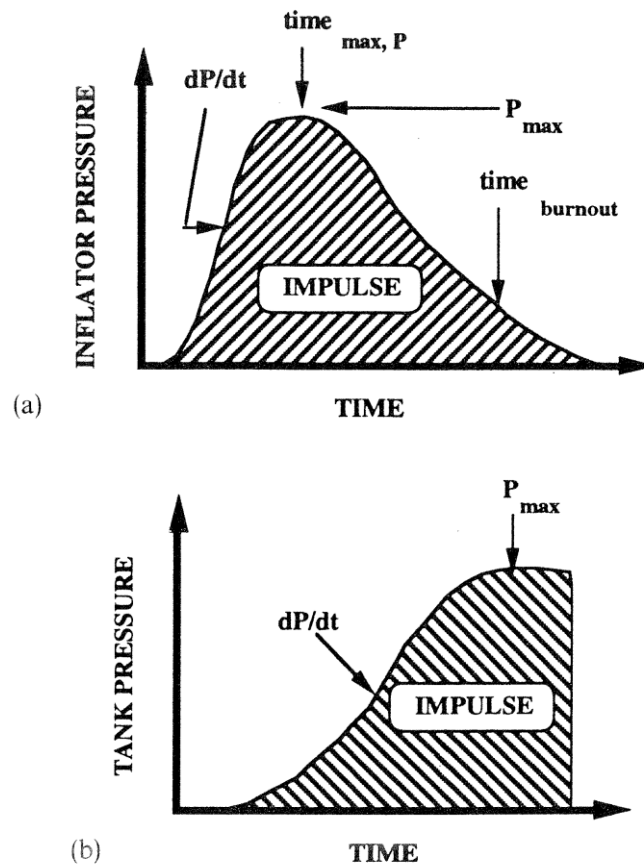
Figure 1.2 Typical pressure profiles for a pyrotechnic inflator.

These inflators work well, but have several major drawbacks including: i) variable performance at high and low ambient conditions due to temperature-dependent surface burn characteristics, ii) the potential for grain fracture and corresponding increased surface area from vehicle vibration/shock over extended periods of time, iii) disposal of un-burnt propellant at the vehicle's end-of-life, and iv) toxicity levels of trace products of combustion (Na, Na_2). In addition, the manufacturing process requires handling and compressive tableting of reactive powdered ingredients used in the production of the propellant grains.

1.4 Hybrid Pyrotechnic Inflators

A design variation of the pyrotechnic inflator is the "hybrid pyrotechnic" inflator. Figure 1.3 illustrates the major components of a passenger-side hybrid pyrotechnic inflator. In brief, it is similar to the pyrotechnic inflator described in the previous section, with the addition of pressurized, inert gas in a plenum (Item A, Fig. 1.3) adjacent to the combustion chamber (Item B, Fig. 1.3). The stored gas serves to augment and dilute the propellant products of combustion, and consequently there is a corresponding reduction in the required amount of propellant to achieve an equivalent discharge as a pure pyrotechnic inflator of greater propellant mass.

The inert gas in a hybrid pyrotechnic inflator is stored at ambient temperature and is mixed with the products of combustion before being discharged into the airbag. Pre-pressurized pyrotechnic inflators demonstrate several advantages over conventional pyrotechnic inflators including: i) reduced propellant mass requirements due to the mass of inert gas stored in the unit, ii) a lower discharge temperature of the gas
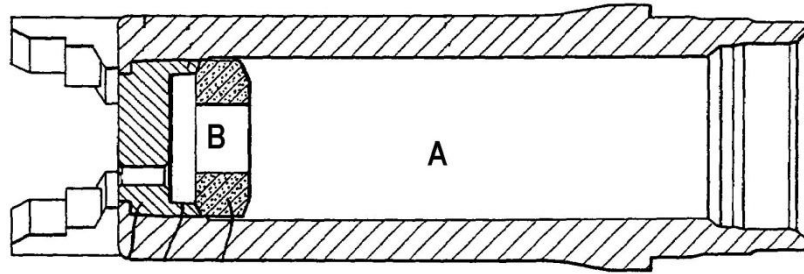
Figure 1.3 Cutaway view of a typical passenger-side hybrid pyrotechnic inflator.

mixture discharged into the airbag (i.e., hot propellant products gas are mixed with ambient temperature stored gas), iii) dilution of unwanted gaseous species produced by the propellant, and iv) the possibility of more uniform performance under "off-design" operating conditions (Schmitt et al., 1997). Nevertheless, the unit still produces unwanted product species and is difficult to manufacture since it combines propellant handling requirements with equipment and procedures for filling high-pressure inflator canisters.

1.5 Heated Gas Inflators

To avoid the propellant-specific disadvantages of pyrotechnic and hybrid pyrotechnic inflators, a third design has been developed that excludes completely the use of solid propellant. These inflators are cylindrical in shape and are initially filled to very high pressure (200 – 500 bar) with a gaseous mixture of fuel and oxidizer. This particular design is referred to as a Heated Gas Inflator (HGI). A more descriptive label would be a Combustible Gas Inflator (CGI) since the "heating" is the result of gas-phase combustion at high pressure. A cutaway view of a typical HGI is shown in Fig. 1.4. In this example, the HGI has an igniter on each end of the canister. The most common fuel is hydrogen,

and the remaining gas is a mixture of oxygen and nitrogen. Trace amounts of helium can also be introduced in the mixture to serve as a detection method for leaks in the canister seals. In the case of a hydrogen-oxygen-nitrogen HGI, the major products of combustion are water vapor, nitrogen and oxygen. Also, the amount of hydrogen is maintained slightly above the lean limit for combustion, yet below lean limit for detonation.

The sequence of events for an HGI is as follows: an HGI is initially filled with a lean mixture of fuel and air to a pressure between 200 and 500 bars. When the inflator is triggered by exceeding the threshold deceleration of the vehicle, the igniter initiates combustion of the fuel and air mixture in the gas molecules adjacent to the igniter. Because the inflator is a cylindrical tube at high initial pressure, the igniter(s) must be mounted in the end walls for structural integrity. Due to the initial conditions of the gaseous mixture, it takes approximately 0.01 seconds for the flame front to propagate the length of the combustion chamber. It should be noted that, in some cases, a second igniter is included on the opposing wall (see, Figure 1.3). At a pre-defined pressure, a burst disk

Figure 1.4 Cutaway view of a typical passenger-side heated gas inflator (HGI).

at one end of the inflator breaks and allows the gas to exit to a small diffuser plenum where the gas is vented through orifices into the airbag. These vents are oriented in a radial fashion so that there is no net force exerted on the HGI.

A unique characteristic of an HGI is that in order to produce enough volume of gas, the inflator has a very high initial pressure. The initial pressure can be as high as 500 bar, and during combustion the bottle pressure can exceed 1,500 bar. At such high pressures the ideal gas assumption, which neglects non-ideal attractive and repulsive forces that the gas particles experience, is no longer valid. Another feature of the HGI is that flame spread through the combustible gas yields pressure waves that propagate at the local speed of sound the length of the tube. These waves, which are inherent to the cylindrical design of the inflator, couple with the flame propagation rate, local pressure oscillations, and gas discharge rate through the nozzle. For example, peak-to-peak pressure excursions have been observed in some test cases to exceed 100 bar. From a design perspective, this creates unique challenges not present in the other inflator designs that exhibit more spatially uniform release of energy during the combustion process.

1.6 Research Objectives

The overall objective of this research is to develop numerical simulation tools capable of modeling the heated gas inflator's temporal and spatial evolution of properties throughout the ignition, combustion and discharge sequence of events ($0 < t < 50$ ms). In order to accomplish this, it is necessary to develop the appropriate governing conservation equations and constitutive relations, implement a suitable numerical scheme, and validate the model. As stated in the previous section, the HGI presents unique challenges. Specifically, the major challenges include: inclusion of real-gas thermodynamics, modeling combustion in a pressure regime with limited/no experimental data, and capturing near-detonation wave dynamics driven by the competing events of combustion and sonic venting. The development of such a

simulation capability will be the first of its kind and therefore contribute to the overall understanding of the HGI functioning and lead to improved designs.

Specific research objectives are:

1) Quantify real-gas thermodynamic states over a range of typical HGI initial conditions.

2) Develop an appropriate form of the field equations and constitutive relations capable of capturing relevant events in HGI functioning.

3) Select and implement a numerical scheme capable of solving the resulting equations in an efficient manner

4) Validate the code by comparing the predicted results for ideal cases with known analytic solutions.

5) Simulate the HGI ballistic cycle for typical operating conditions.

CHAPTER 2

MATHEMATICAL FORMULATION

2.1 Introduction

Accurately simulating the complete HGI ballistic cycle from the moment of ignition through combustion and eventual discharge of all inflator gas into the airbag is a complex process that includes a number of coupled, non-ideal processes. For the research presented herein, the following assumptions were applied in the development of the governing equations and constitutive relations:

1) Gravity forces are neglected.

2) Species mass and thermal diffusion are neglected.

3) Flow is highly compressible.

4) Viscosity is neglected.

5) Thermodynamic states can be non-ideal.

6) The combustion canister is axisymmetric.

7) The gas is a mixture of different chemical species, each with temperature-dependent specific heat.

Given these assumptions, governing conservation equations and corresponding constitute relations were developed for a continuum field representing the interior of the inflator canister. The following sections outline the resulting mathematical formulations. The numerical solution method is described in the following chapter.

2.2 Gas-Phase Flow Field

Shown below are the forms of the Euler form of the conservation equations

(Ramadan and Butler, 2003) used in this work.

Continuity Equation:

$$\frac{\partial \rho}{\partial t} + \nabla \cdot (\rho V) = 0 \tag{2.1}$$

Momentum Equation:

$$\frac{\partial (\rho V)}{\partial t} + \nabla \cdot (\rho V \otimes V + P) = 0 \tag{2.2}$$

Energy Equation:

$$\frac{\partial E}{\partial t} + \nabla \cdot [(E + P)V] = 0 \tag{2.3}$$

Species Conservation Equation:

$$\frac{\partial (\rho Y_k)}{\partial t} + \nabla \cdot (\rho Y_k V) = \omega_k \tag{2.4}$$

In the above equations, the mixture total energy E is given by:

$$E = \rho u + \frac{1}{2} \rho V \cdot V \tag{2.5}$$

where u is defined as the mixture specific internal energy, that does not include chemical

energy. In Eq. (2.4) Y_k and ω_k are the mass-fraction and mass production rate of the k-th

species, respectively. Species and mixture properties are related through standard mass-,

or molar-based mixing rules.

The above conservation equations are rewritten for an axisymmetric coordinate

system.

$$\frac{\partial \rho}{\partial t} + \frac{\partial(\rho V_x)}{\partial x} + \frac{\partial(\rho V_y)}{\partial y} = -\frac{\rho V_y}{y} \tag{2.6}$$

$$\frac{\partial(\rho V_x)}{\partial t} + \frac{\partial(\rho V_x^2 + P)}{\partial x} + \frac{\partial(\rho V_x V_y)}{\partial y} = -\frac{\rho V_x V_y}{y} \tag{2.7}$$

$$\frac{\partial(\rho V_y)}{\partial t} + \frac{\partial(\rho V_x V_y)}{\partial x} + \frac{\partial(\rho V_y^2 + P)}{\partial y} = -\frac{\rho V_y^2}{y} \tag{2.8}$$

$$\frac{\partial E}{\partial t} + \frac{\partial[V_x(E+P)]}{\partial x} + \frac{\partial[V_y(E+P)]}{\partial y} = -\frac{V_y(E+P)}{y} \tag{2.9}$$

$$\frac{\partial(\rho Y_k)}{\partial t} + \frac{\partial(\rho V_x Y_k)}{\partial x} + \frac{\partial(\rho V_y Y_k)}{\partial y} = -\frac{\rho V_y Y_k}{y} + \omega_k \tag{2.10}$$

Equations (2.6) through (2.10) can be rewritten in vector form as:

$$\frac{\partial U}{\partial t} + \frac{\partial F(U)}{\partial x} + \frac{\partial G(U)}{\partial y} = S(U) \tag{2.11}$$

where U represents the array of conservative variables, F(U) and G(U) represent the flux terms in the axial and radial direction, and S(U) represents the source terms.

$$
U = \begin{bmatrix} \rho \\ \rho V_x \\ \rho V_y \\ E \\ \rho Y_k \end{bmatrix}, \quad
F(U) = \begin{bmatrix} \rho V_x \\ \rho V_x^2 + P \\ \rho V_x V_y \\ V_x(E+P) \\ \rho V_x Y_k \end{bmatrix}, \quad
G(U) = \begin{bmatrix} \rho V_y \\ \rho V_x V_y \\ \rho V_y^2 + P \\ V_y(E+P) \\ \rho V_y Y_k \end{bmatrix} \tag{2.12}
$$

$$
S(U) = \begin{bmatrix} -\rho V_y / y \\ -\rho V_x V_y / y \\ -\rho V_y^2 / y \\ -V_y(E+P)/y \\ -\rho V_y Y_k / y + \omega_k \end{bmatrix}
$$

The additional terms appearing in the vector S(U) represent the geometric source terms that result from converting the system of equations from Cartesian to an axisymmetric coordinate system.

2.3 Species Production Rates

The present work incorporates a real-gas adaptation (Schmitt and Butler, 1995a) of standard elementary reaction modeling with Arrhenius kinetics (Kee et al., 1980). In order to calculate the production rate ω_k of the k-th species appearing in the governing equations, it is first necessary to define the nomenclature and form of a general set of elementary reactions as:

$$\sum_{k=1}^{KK} v_{ki}' \chi_k \Leftrightarrow \sum_{k=1}^{KK} v_{ki}'' \chi_k \qquad (i=1,\ldots II) \qquad (2.13)$$
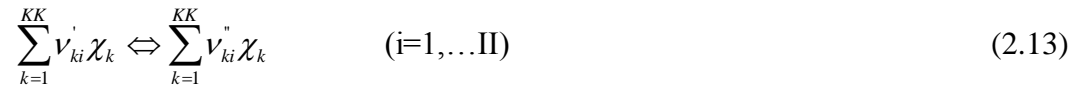
where v_{ki} represents the i-th reaction's stoichiometric coefficient and χ_k represents the chemical symbol for the k-th species. Knowing the form of the reaction set being considered, one can express the production rate of the k-th species as:

$$\omega_k = W_k \sum_{i=1}^{II} \left(v_{ki}'' - v_{ki}' \right) q_i \qquad (2.14)$$

The rate of progress variable, q_i, for the i-th reaction is given by the difference of the forward and reverse rates as,

$$q_i = k_{fi} \prod_{k=1}^{KK} [X_k]^{v_{ki}'} - k_{rii} \prod_{k=1}^{KK} [X_k]^{v_{ki}''} \qquad (2.15)$$

Here, the forward reaction rate constant is calculated using a standard Arrhenius form:

$$k_{fi} = A_i T^{\beta_i} \exp(-E_i / R_c T) \qquad (2.16)$$

In Eq. (2.16) the constants A_i, β_i and E_i are respectively, the pre-exponential factor, the temperature exponent, and the activation energy. These are usually determined experimentally at low pressure and therefore are possibly in error when used at the extreme high pressures experienced in HGIs.

In order to achieve the thermodynamically correct equilibrium state under non-ideal conditions, the reverse rate k_{ri} is determined using the forward rate k_{fi} and a form of the equilibrium constant that is consistent with the chosen form of the non-ideal equation of state:

$$K_{ci} = \frac{k_{fi}}{k_{ri}} \tag{2.17}$$

The details of how this equilibrium constant is calculated are beyond the scope of this research, but can be found in detail in Schmitt (1994).

<div align="center">2.4 Mass Discharge Rate</div>

Depending on the pressure differential across the plane of the exit orifices, mass flow rates leaving the inflator can be either subsonic or sonic. This is done by checking the ratio of the pressures on either side of the nozzle to determine if the ratio exceeds the critical choked flow condition (Zucrow and Hoffman, 1976). This critical ratio is calculated as:

$$P_{cr} = \left(\frac{2}{\gamma - 1}\right)^{\frac{\gamma}{\gamma - 1}} \tag{2.18}$$

Once the flow condition is determined, the correct function for the mass flow rate can be used. If the flow is subsonic the mass flow rate is calculated using:

$$\dot{m} = A_{flow}\sqrt{\frac{2\gamma}{\gamma - 1}P_+\rho_+\left(P_\pm^{2/\lambda} - P_\pm^{\gamma+1/\gamma}\right)} \tag{2.19}$$

where $P_{\pm}=P_{+}/P_{-}$, and P_{+} and P_{-} are respectively the high and low pressures of the gas on nozzle's interior and exterior.

If the flow is found to be sonic, the properties of the gas leaving the inflator are independent of the exterior state (i.e., airbag interior). Given a sonic exit condition, the following equation is used to find the stagnation temperature of the fluid at the exit plane:

$$T_{o1} = T_1\left(1 + \frac{\gamma-1}{2}M_1^2\right) \tag{2.20}$$

where T_1 is the local static temperature, and Mach number is calculated as:

$$M = \frac{\sqrt{V_x^2 + V_y^2}}{c} \tag{2.21}$$

with u, v, and c being respectively, the x-velocity, y-velocity, and the speed of sound of the gas at the exit plane. Knowing the stagnation temperature, it is possible to determine the static temperature at the nozzle exit location. Seeing as the Mach number at the exit is always unity, and that $T_{o,nozzle} = T_{o1}$, the equation for T_{nozzle} becomes:

$$T_{nozzle} = T_{o1}\bigg/\left(1 + \frac{\gamma-1}{2}M_{nozzle}^2\right) \tag{2.22}$$

Combining Eqs. (2.19) and (2.22) and setting $M_{nozzle} = 1$ gives:

$$T_{nozzle} = T_1\left(1 + \frac{\gamma-1}{2}M_1^2\right)\bigg/\left(1 + \frac{\gamma-1}{2}\right) \tag{2.23}$$

Similar calculations can be performed for pressure and density. Equations for P_{nozzle} and ρ_{nozzle} can be seen below.

$$\rho_{nozzle} = \rho_1\left(1 + \frac{\gamma-1}{2}M_1^2\right)^{\frac{1}{\gamma-1}}\bigg/\left(1 + \frac{\gamma-1}{2}\right)^{\frac{1}{\gamma-1}} \tag{2.24}$$

$$P_{nozzle} = P_1 \left(1 + \frac{\gamma-1}{2} M_1^2\right)^{\frac{\gamma}{\gamma-1}} \bigg/ \left(1 + \frac{\gamma-1}{2}\right)^{\frac{\gamma}{\gamma-1}} \qquad (2.25)$$

Now that the density at the nozzle is known, the mass flow rate out of the continuum can

be calculated as:

$$\dot{m}_o = A_{nozzle} \rho_{nozzle} c \qquad (2.26)$$

Once T_{nozzle} and P_{nozzle} are known, it is possible to calculate the energy leaving the system

as:

$$\dot{m}_o h_o = \dot{m}_o (h_{nozzle} + 0.5c^2) \qquad (2.27)$$

<u>2.5 Real Gas Equations of State</u>

Based on the high pressure states expected in HGI simulations, the perfect gas

assumption (PV = mRT) fails to accurately represent the system's thermodynamic states.

In fact, the initial conditions for an HGI initially pressurized to 400 bar is in error by as

much as 25% if the perfect gas assumption is assumed. Furthermore, during the firing

cycle the peak inflator pressure can reach as high as 2,000 – 3,000 bar. Therefore, it is

necessary to develop the system of governing equations using non-ideal (or, "real-gas")

thermodynamics. The form of a real gas equation of state is similar to that of the ideal gas

equation, except that it includes a compressibility term Z, shown in the equation below:

$$PV = mRTZ \qquad (2.28)$$

The compressibility factor is a complex function that is added to adjust the state

calculations to include non-ideal attractive and repulsive forces that particles experience

at high temperatures and pressures. A non-unity compressibility factor also affects the

form of other thermodynamic properties. For example, the enthalpy of an ideal gas is independent of pressure (i.e., H = H(T)), whereas the enthalpy of non-ideal gases depends on both temperature and pressure (i.e., H = H(T, P)).

The compressibility function of a non-ideal gas must accurately represent the entire operating regime of the species contained in the mixture. The real gas equations of state proposed by van der Waals, Redlich-Kwong, Soave, and Peng-Robinson (Bergan, 1991) have been shown to work well for reactive mixtures similar in composition to HGI mixtures. All of these equations of state take the form of a cubic equation with compressibility as the independent variable. The basic form of a cubic equation of state is,

$$Z^3-(1+B^*-uB^*)Z^2+(A^*+wB^{*2}-uB^*-uB^{*2})Z-A^*B^*-wB^{*2}-wB^{*3}=0 \qquad (2.29)$$

Where the non-dimensional attraction term is:

$$A^* = \frac{a_m P}{R^2 T^2} \qquad (2.30)$$

And, the non-dimensional repulsive term is:

$$B^* = \frac{b_m P}{RT} \qquad (2.31)$$

Mixing rules are used to find a_m and b_m, and are given as

$$a_m = \sum_{i=1}^{KK}\sum_{j=1}^{KK} X_i X_j (a_i a_j)^{1/2} \qquad (2.32)$$

and

$$b_m = \sum_{i=1}^{KK} X_i b_i \qquad (2.33)$$

The remaining constants for the various forms of the cubic equations of state can be found in Table 2.1.

Table 2.1 Constants for Cubic Equations of State

Equation of State	u	w	b	a
van der Waals	0	0	$\dfrac{RT_c}{8P_c}$	$\dfrac{27}{64}\dfrac{R^2T_c^2}{P_c}$
Redlich-Kwong	1	0	$\dfrac{0.08664RT_c}{P_c}$	$\dfrac{0.42748R^2T_c^{2.5}}{P_cT^{0.5}}$
Soave	1	0	$\dfrac{0.08664RT_c}{P_c}$	$\dfrac{0.42748R^2T_c^{2.5}}{P_c}[1+f_\omega(1-T_r^{0.5})]^2$ where f_ω=0.48+1.574ω-0.176ω^2
Peng-Robinson	2	-1	$\dfrac{0.07780\,RT_c}{P_c}$	$\dfrac{0.42748R^2T_c^{2.5}}{P_c}[1+f_\omega(1-T_r^{0.5})]^2$ where f_ω=0.48+1.574ω-0.176ω^2

2.6 Species Thermodynamic Data at Standard State

To calculate specific enthalpy and internal energy, specific heat at standard state (P = 1 bar) of species k is calculated using,

$$\frac{C_{pk}^o}{R} = a_{1k} + a_{2k}T + a_{3k}T^2 + a_{4k}T^3 + a_{5k}T^4 \tag{2.34}$$

where all a_{nk} coefficients are from standard JANNAF thermodynamic data. The corresponding enthalpy at standard state of species k is calculated using the basic thermodynamic expression,

$$H_k^o(T) = \int_0^T C_{pk}^o(T)\,dT \tag{2.35}$$

Because of the polynomial form of Eq. (2.34), the non-dimensional species enthalpy can be rewritten in the form,

$$\frac{H_k^o(T)}{RT} = \sum_{n=1}^{5}\left[n^{-1}a_{nk}T^{(n-1)}\right] + \frac{a_{6k}}{T} \tag{2.36}$$

For reference, the product of a_{6k} and R yield the enthalpy of formation at standard state.

The mixture enthalpy at the reference state can be expressed by standard mixing rules as:

$$H^o\left(T, P_o, X\right) = \sum_{k=1}^{KK} X_k H^o_k \tag{2.37}$$

2.7 Mixture Properties at Non-Ideal States

The gaseous mixture properties are computed in the software package Chemkin

Real Gas (Schmitt and Butler, 1995b) with reference to the species properties at standard

state (see, previous section) and a cubic form of the non-ideal equation of state. The

deviation from ideal state is often referred to as the departure function or non-ideal

residual. Using the previously defined cubic form of the equation of state (Eq. (2.29)), the

mixture departure functions for enthalpy take the following forms (Butler and Schmitt)

van der Walls;

$$H(T, P, X) - H^o\left(T, P_o, X\right) = \frac{-a_m P}{ZRT} + RT(Z - 1) \tag{2.38}$$

Redlich-Kwong, Soave, and Peng-Robinson;

$$H(T, P, X) - H^o\left(T, P_o, X\right) = \left(\frac{3}{2}\frac{a_m}{b_m}\right)\ln\left(\frac{Z}{Z + B^*}\right) + RT(Z - 1) \tag{2.39}$$

Once the real-gas mixture enthalpy is known, the real-gas mixture internal energy can be

found using:

$$U = H - RTZ \tag{2.40}$$

CHAPTER 3

NUMERICAL SOLUTION METHOD

3.1 General Solution Method

The numerical method used in this research was originally developed by (Toro, 1999) and later adapted by (Ramadan, 2002) for his work on modeling pulsed detonation thermal spray devices. In order to accurately handle the sharp change in species at the combustion front and shock waves propagating through the inflator's combustion chamber, a high resolution shock capturing technique was needed. The method used in this research was developed specifically to solve the conservation form of the governing equations for flows with shock waves. Using a numerical scheme that is capable of handling the sharp discontinuities of shock waves will also give the code the ability to properly solve the steep gradients in composition that appear at the combustion/detonation front.

The homogeneous part of the governing equations is solved by a Flux Vector Splitting technique and a total variation diminishing (TVD) property (Toro, 1999 and Hirsch, 1989). Since the governing partial differential equations for this model are non-homogeneous, the homogeneous and non-homogeneous parts of the equations are solved separately by mathematically "splitting" the equations into two distinct sets of idealized equations. The solutions from each sub-solution are then coupled using a time splitting method to complete a single step forward in time. The non-homogeneous part of the equations becomes a set of ordinary differential equations (ODEs) that can be solved using a standard ODE algorithm. The ODE solver used in this research is the Livermore Solver for Ordinary Differential Equations (LSODE).

3.2 The Time Splitting Method

The general vector form of the governing equations are written as:

$$\frac{\partial U}{\partial t} + \frac{\partial F(U)}{\partial x} + \frac{\partial G(U)}{\partial y} = S(U) \qquad (3.1)$$

Where U, F(U), G(U) and S(U) are:

$$U = \begin{bmatrix} \rho \\ \rho V_x \\ \rho V_y \\ E \\ \rho Y_k \end{bmatrix}, \qquad F(U) = \begin{bmatrix} \rho V_x \\ \rho V_x^2 + P \\ \rho V_x V_y \\ V_x(E+P) \\ \rho V_x Y_k \end{bmatrix}, \qquad G(U) = \begin{bmatrix} \rho V_y \\ \rho V_x V_y \\ \rho V_y^2 + P \\ V_y(E+P) \\ \rho V_y Y_k \end{bmatrix} \qquad (3.2)$$

$$S(U) = \begin{bmatrix} -\rho V_y / y + \dot{m}_o \\ -\rho V_x V_y / y \\ -\rho V_y^2 / y \\ -V_y(E+P)/y + \dot{m}_o h_o \\ -\rho V_y Y_k / y + \dot{m}_o Y_k + \omega_k \end{bmatrix}$$

Dropping the source terms gives the homogeneous form of the equations,

$$\frac{\partial U}{\partial t} + \frac{\partial F(U)}{\partial x} + \frac{\partial G(U)}{\partial y} = 0 \qquad (3.3)$$

which is solved using the flux vector splitting technique. The remaining non-homogeneous terms are written as follows:

$$\frac{\partial U}{\partial t} = S(U) \qquad (3.4)$$

and is solved using the ODE solver LSODE.

The procedure used in this research has second-order accuracy in time. With the initial condition $U(x, y, t^n) = U^n$ the solution U^{n+1} is found using:

$$U^{n+1} = C^{(\Delta t/2)} S^{(\Delta t)} C^{(\Delta t/2)}(U^n) \qquad (3.5)$$

where the C (i.e., "convective") and S (i.e., "source") operators appearing in Equation (3.5) represent the solution of Eqs. (3.3) and (3.4), respectively.

In Equation (3.5), the solution methodology is best understood by interpreting the layered expression from right to left. That is, the solution sequence proceeds as follows:

$$U^{step1} = C^{(\Delta t/2)}(U^n) \qquad (3.5a)$$

$$U^{step2} = S^{(\Delta t)}(U^{step1}) \qquad (3.5b)$$

$$U^{n+1} = C^{(\Delta t/2)}(U^{step2}) \qquad (3.5c)$$

3.3 Flux Vector Splitting

The Flux Vector Splitting technique used in this research is the same as used by Ramadan (2002) in his research on Detonation Thermal Spraying. The basic form of a one-dimensional Flux Vector Splitting scheme (Steger and Warming, 1981) is written as:

$$\frac{\partial U}{\partial t} + \frac{\partial F^+}{\partial x} + \frac{\partial F^-}{\partial x} = 0 \qquad (3.6)$$

where F^+ is the flux calculated with a rearward difference scheme and uses only information upstream of the location. Similarly, F^- is calculated using a forward difference scheme and uses only downstream information. The Flux Vector Splitting method used in this research uses advanced techniques to properly solve the fluxes for flows with shock waves. A description of the detailed step-by-step equations for Flux Vector Splitting method in two-dimensions can be found in Appendix A. The equations shown in Appendix A represent the exact form of the solution algorithm employed in this research.

3.4 The Runge-Kutta TVD Scheme

Equation (A.63), developed using the Flux Vector Splitting technique described in detail in Appendix A, is solved using a second-order Runge-Kutta scheme (Shu and Osher, 1988). This scheme is developed to be Total Variation Diminishing (TVD). Equations of the form:

$$\frac{\partial u}{\partial t} + \frac{\partial f}{\partial x} = 0 \tag{3.7}$$

have the property that $\left| \partial u / \partial x \right|$ integrated over the entire domain will not increase with time. Setting $L(U)$ equal to the right hand side of Eq. (A.63), the second order Runge-Kutta scheme is solved as:

$$\overline{U} = U^n + \Delta t * L(U^n) \tag{3.8}$$

$$U^{n+1} = \frac{1}{2}(U^n + \overline{U}) + \frac{1}{2}\Delta t * L(\overline{U}) \tag{3.9}$$

The time step Δt for stability reasons is determined by using the Courant-Friedrichs-Lewy (CFL) condition. The CFL condition is calculated as follows:

$$(\Delta t)^t = \frac{\Delta x}{c^t + u^t} \tag{3.10}$$

where u and c are the local velocity and speed of sound, respectively. The CFL condition is calculated by using the highest value of $c + u$ in both the axial and radial direction over the time step. This method produces a time step that will produce a stable solution for flows with shock waves. In order to guarantee that the solution will be stable and that the time step is small enough for the source terms solved in the ODE solver, the time step used in this research is conservatively chosen as one half of the CFL condition.

<u>3.5 Boundary Conditions</u>

Figure 3.1 is a representation of the continuum model created for the combustion

chamber of an HGI. Since the problem is symmetric only half of the domain is
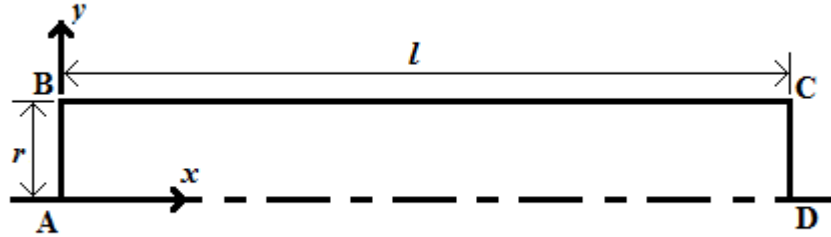
considered.

Figure 3.1 Schematic of the computational domain

Only one type of boundary condition is needed for the HGI inflator cylindrical

geometry. All of the walls (AB, BC, and CD) and the center line (AD) will be treated as

reflective boundary conditions. In order to achieve this condition it is necessary to have a

zero velocity in the normal direction at the boundary. To achieve the zero velocity

condition it is necessary to force the fluxes at each boundary to be zero. This is done by

using the following conditions for two fictitious points outside of each boundary:

Continuity:	$\rho(3) = \rho(0)$,	$\rho(2) = \rho(1)$
X - Momentum:	$V_x(3) = -V_x(0)$,	$V_x(2) = -V_x(1)$
Y - Momentum:	$V_y(3) = V_y(0)$,	$V_y(2) = V_y(1)$
Energy:	$E(3) = E(0)$,	$E(2) = E(1)$
Species:	$\rho Y_k(3) = \rho Y_k(0)$,	$\rho Y_k(2) = \rho Y_k(1)$

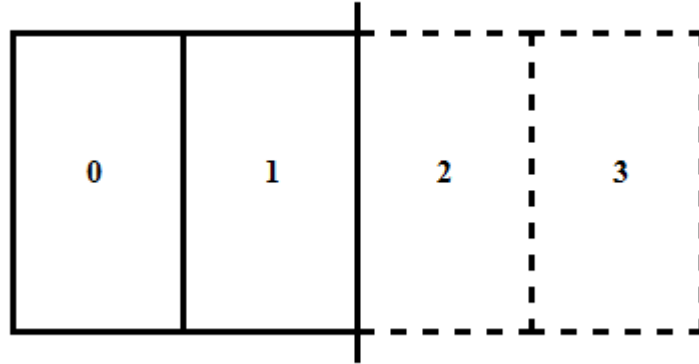A depiction of the fictitious cells can be seen below in Figure 3.2.

Figure 3.2 Cell depiction at boundaries

These condition transform into the following flux conditions:

Continuity:
$$F^-(3) = -F^+(0), \qquad F^+(3) = -F^-(0)$$
$$F^-(2) = -F^+(1), \qquad F^+(2) = -F^-(1)$$

X - Momentum:
$$F^-(3) = F^+(0), \qquad F^+(3) = F^-(0)$$
$$F^-(2) = F^+(1), \qquad F^+(2) = F^-(1)$$

Y - Momentum:
$$F^-(3) = -F^+(0), \qquad F^+(3) = -F^-(0)$$
$$F^-(2) = -F^+(1), \qquad F^+(2) = -F^-(1)$$

Energy:
$$F^-(3) = -F^+(0), \qquad F^+(3) = -F^-(0)$$
$$F^-(2) = -F^+(1), \qquad F^+(2) = -F^-(1)$$

Species:
$$F^-(3) = -F^+(0), \qquad F^+(3) = -F^-(0)$$
$$F^-(2) = -F^+(1), \qquad F^+(2) = -F^-(1)$$

3.6 Overall Numerical Procedure

In summary, the overall numerical procedure for the solution of the governing equations is as follows:

(1) The code first determines the proper Δt for this time step by solving Eq. (3.10) in both the axial and radial direction. The homogeneous part of the governing equations is then solved for half a time step using the two step Runge-Kutta method described in Section 3.4. This solution yields an intermediate solution of the conserved variables. From the conserved variables the density, velocity, internal energy, and mass fraction for each cell are determined from the constitutive relations. Using these primitive variables it is then possible to calculate the gas temperature and pressure using the chosen real gas equation of state.

(2) The remaining non-homogeneous parts of the governing equations include the combustion, venting, and geometric source terms. These are solved for a complete time step using the ODE solver LSODE. The initial conditions for the solver come from the solution of the two step Runge-Kutta scheme in step (1). The temperature, pressure and other gas properties are again calculated as described in step (1).

(3) Eq. (3.10) is solved again for a half step using the Runge-Kutta method in step one. This time the initial conditions are the output from step (2). The output from this step is then stored as the solution for one complete time step.

CHAPTER 4

VALIDATION

4.1 Introduction

This chapter presents results for four unique test cases used to validate the governing equations and the numerical method chosen to simulate the HGI ballistic cycle. The four test cases are as follows:

1. Test Case 1 - Shock Tube: This case provides a test of the Euler form of the governing equations as well as the numerical solution algorithm in resolving a shock discontinuity as it propagates through the HGI domain. Assuming the fluid is an ideal gas with constant specific heat, an exact theoretical solution exists and can be used for direct comparison with the code's numerical solution. In addition to matching the theoretical wave speeds, the HGI code must also resolve the shock thickness to an acceptable level.

2. Test Case 2 - Constant Volume Explosion: Here, the form of the real-gas equation of state, mass-production rate, and conservation of energy equations are tested using a constant-volume reaction case where the reactants undergo transformation through a set of elementary reactions to final equilibrium products. Again, a theoretical solution exists from equilibrium theory that can be used for comparison with the numerical solution.

3. Test Case 3 - Isentropic Venting: This test case compares the theoretical rate of sonic venting from a well-mixed chamber with the solution generated from the HGI simulation code. Again, under ideal assumptions an exact theoretical solution is obtainable.

4. Test Case 4 - Detonation: Replicating the theoretical solution for a steady-state gaseous detonation by solving the time-dependent form of the conservation equations presents a unique test of several features of the solution methodology. The simulation must accurately reproduce the dynamics (i.e., wave speed) as well as the shock thickness and thermodynamic states of the products.

4.2 Test Case 1 - Shock Tube

The shock tube problem is a common case that is often used to determine a CFD code's ability to handle shock waves. A shock tube consists of a closed, elongated tube that is divided into high and low pressure regions by a diaphragm. In Fig. 4.1, the high-pressure region is designated as 4, whereas the low-pressure region is designated as 1.
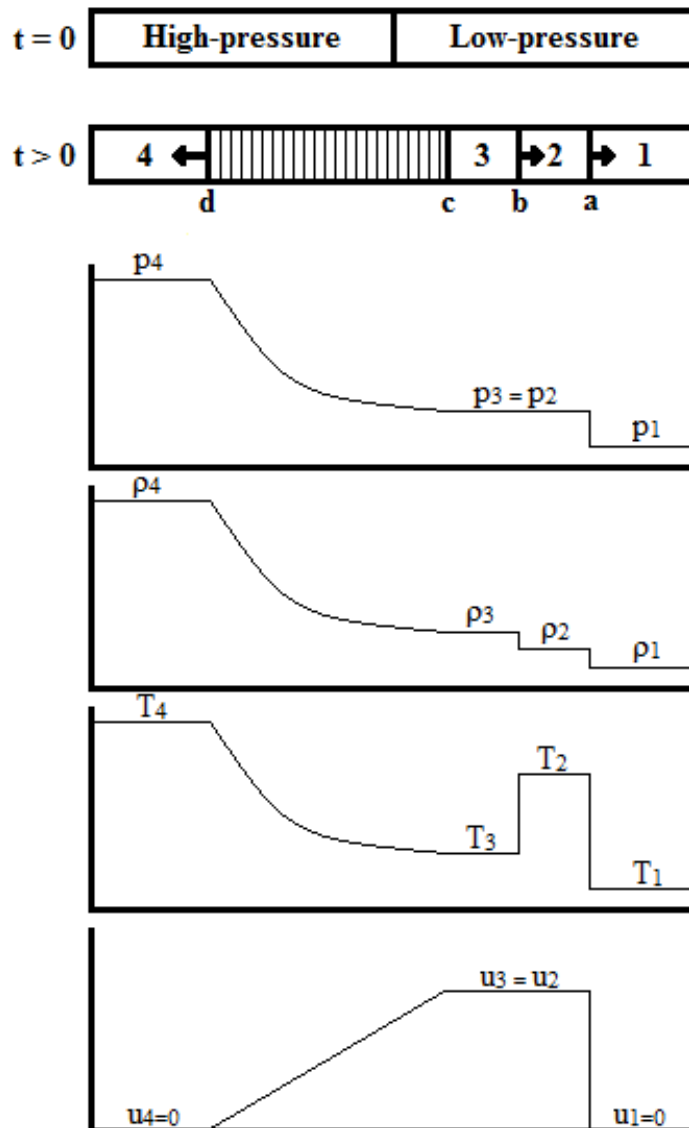

Figure 4.1 Illustration of Test Case 1 - Shock Tube.

At time t = 0, the diaphragm separating the high- and low-pressure regions is broken and an initial pressure discontinuity (P_2/P_1) propagates left-to-right into the low-pressure region. The wave travels at supersonic speed. This wave can be seen in Fig. 4.1 labeled as 'a'. At the same time, an expansion wave moves right-to-left into the high-pressure region. The head wave 'd' and tail wave 'c' both move at the local speeds of sound of region 4 and region 3, respectively. For a full description of the analytical solution to the perfect-gas, constant specific heat shock tube case, see Appendix B.

For this validation study, the shock tube is filled with argon with a constant specific heat ratio of $\gamma = 1.66$. This test case was selected in order to compare with the analytic solution which also assumes a constant specific heat. For the test case, the high-pressure region has the initial conditions of p = 163.68 atm and T = 1,900 K. The low pressure side has p = 1 atm and T = 300 K. The numerical grid size used in this study was $\Delta x = 0.25$ mm.

The results for the study are compared at t = 0.1 ms in Figs. 4.2 - 4.7. The pressure profiles in Figs. 4.2 and 4.3 illustrate that the shock wave discontinuity is captured in approximately 6 grid points, or 1.5mm. The closer view seen in Fig. 4.3 displays that the magnitude of the shock is predicted very accurately. The contact discontinuity, seen only in the density and temperature plots, appears to have quite a bit of smearing. Despite the smearing, the position and magnitude of the contact discontinuity match the theoretical solution very well. The plots also show that the expansion region, the head expansion wave, and tail expansion wave all compare very well with the theoretical solution.
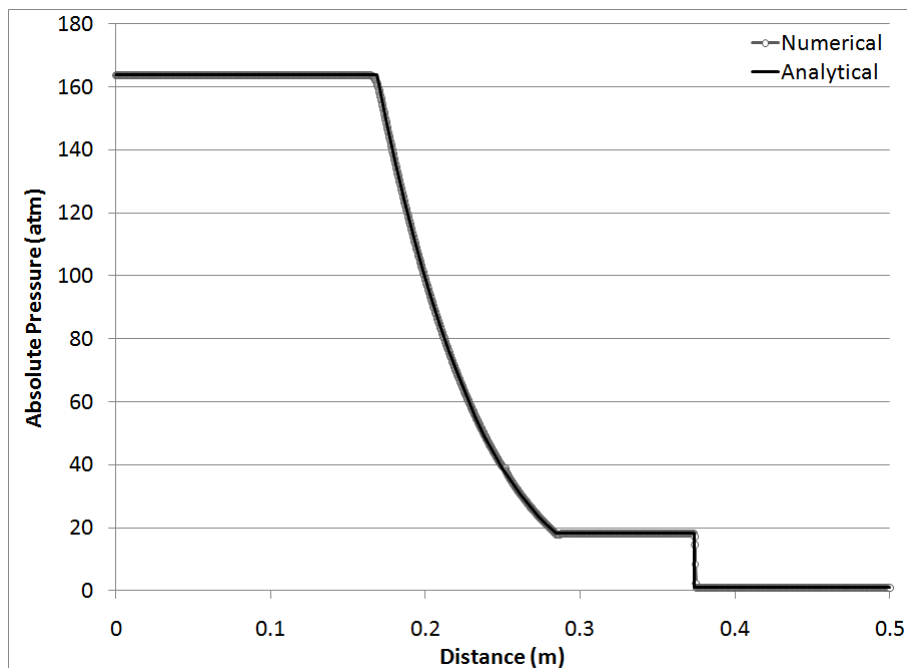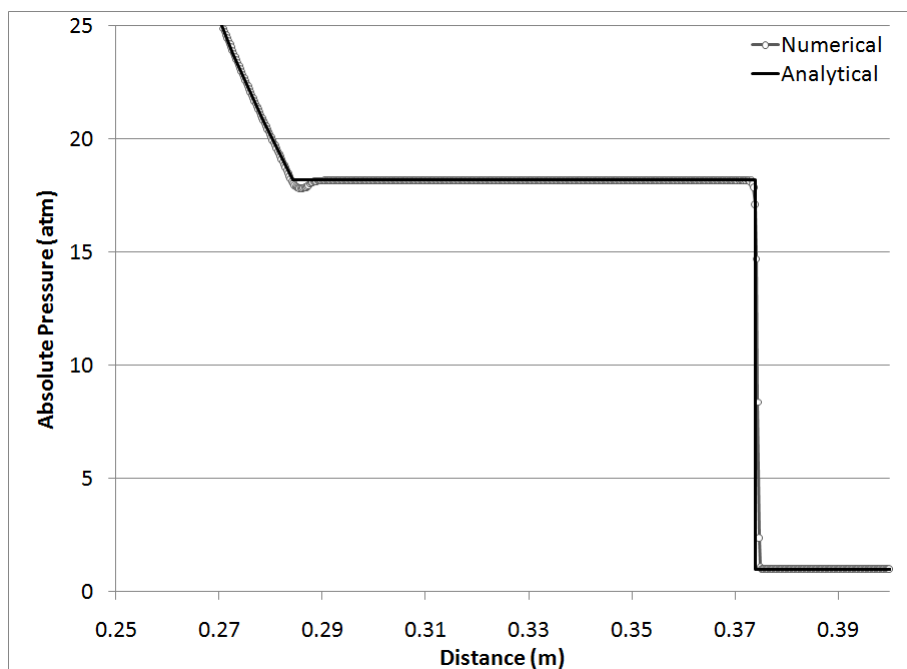
Figure 4.2 Shock Tube: Absolute pressure at t = 0.1 ms.

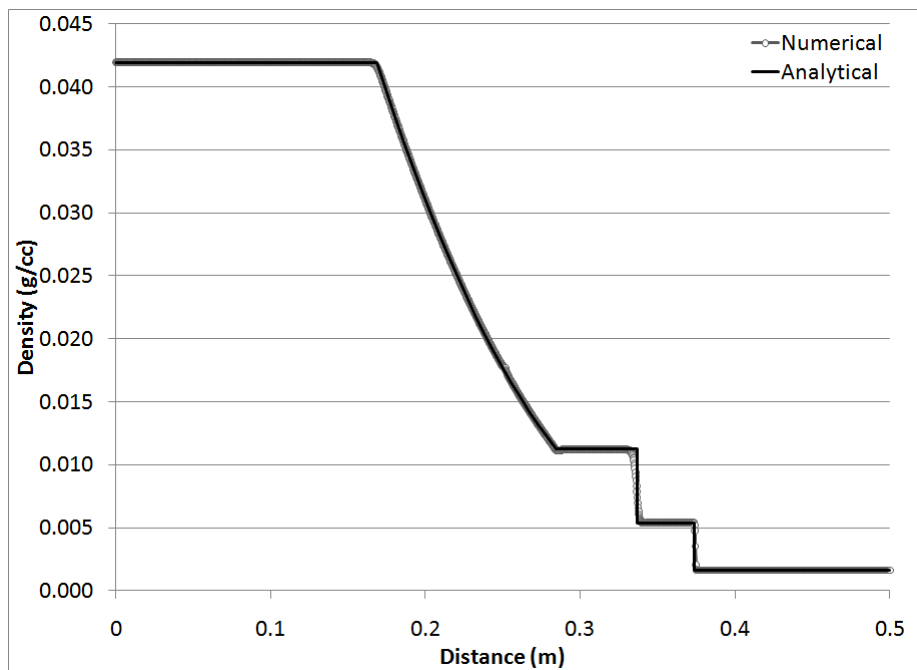Figure 4.3 Shock Tube: Enlarged view of absolute pressure at t = 0.1 ms.
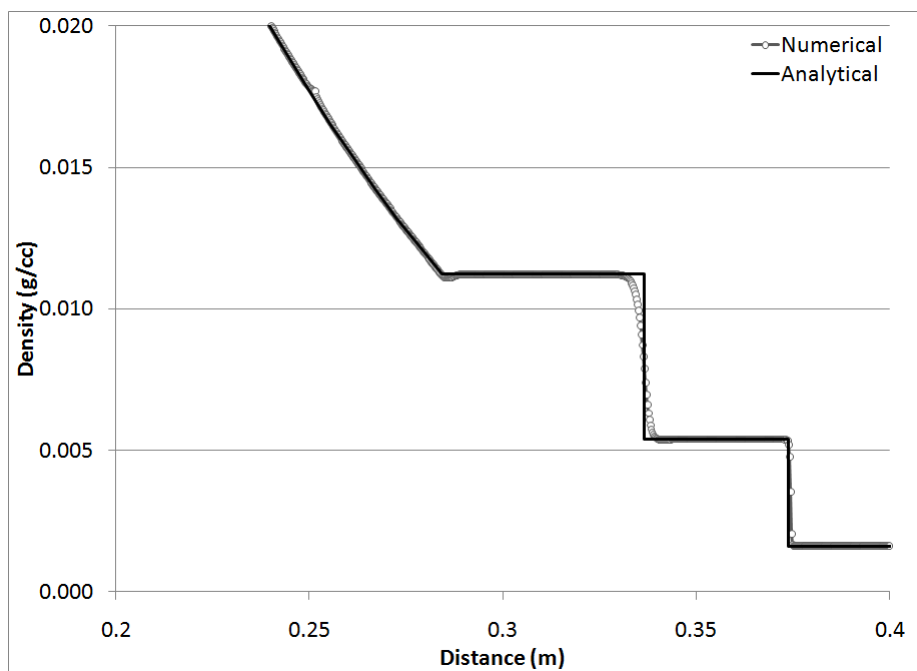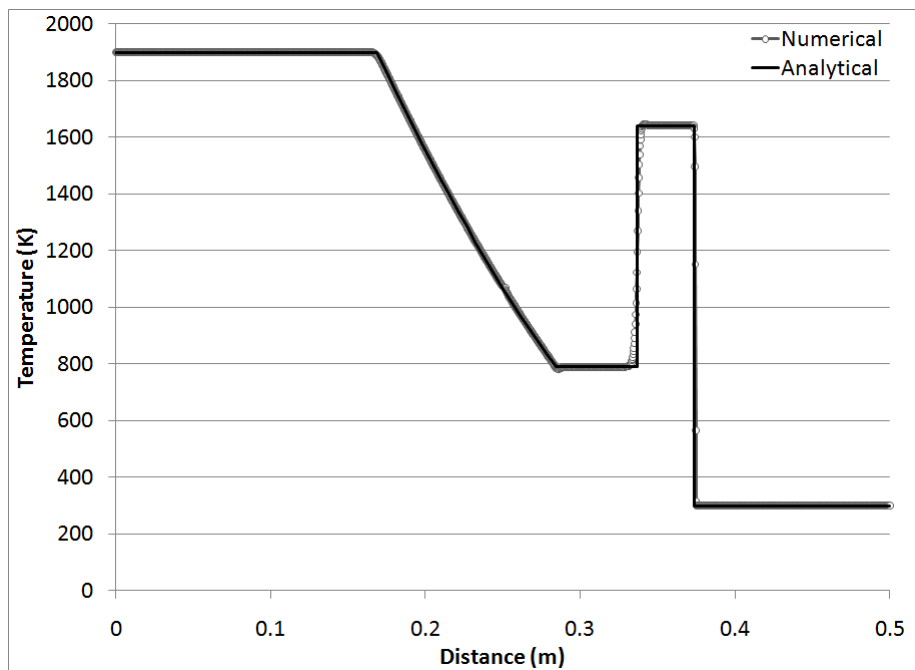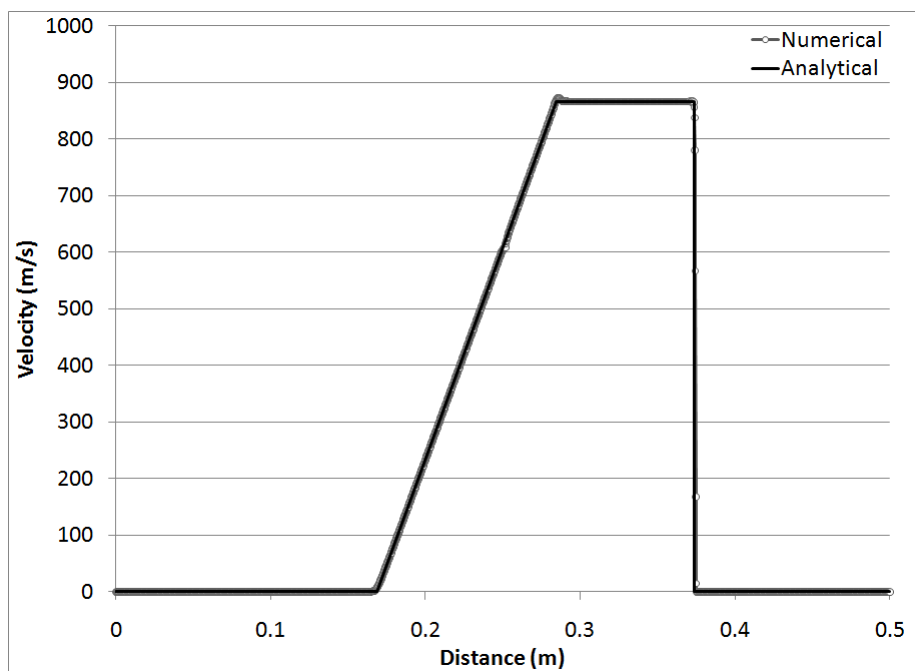
Figure 4.4 Shock Tube: Density at t = 0.1 ms.

Figure 4.5 Shock Tube: Enlarged view of density at t = 0.1 ms.

Figure 4.6 Shock Tube: Temperature at t = 0.1 ms.

Figure 4.7 Shock Tube: Velocity at t = 0.1 ms.

4.3 Test Case 2 – Constant-volume Explosion

The constant-volume explosion study was done to check the HGI simulation code's ability to accurately predict the final equilibrium state for a reactive mixture undergoing a change in chemical composition in an adiabatic, constant-volume process. The initial conditions for this study are listed in Table 4.1.

Table 4.1 Test Case 2: Initial conditions

Temperature (K)	300
Pressure (atm)	400
Mass % -H2	0.01297
Mass % - O2	0.23000
Mass % - N2	0.75700
Mass % - H2O	0.00000
Mass % - OH	0.00000

The study was performed using both the ideal and real gas equations of state. The predicted final state for each equation of state is given in Tables 4.2 - 4.5. The data from each of the cases shows that the HGI code was able to accurately reproduce the final state predicted by equilibrium theory (RGEQUIL).

Table 4.2 Constant-volume Explosion: Final state - Ideal Gas EOS

	Theory	Model
Temperature (K)	1875.2	1875.2
Pressure (atm)	2302.4	2302.4
Mass % -H2	8.7004E-08	8.6993E-08
Mass % - O2	1.2697E-01	1.2697E-01
Mass % - N2	7.5705E-01	7.5705E-01
Mass % - H2O	1.1587E-01	1.1587E-01
Mass % - OH	1.1060E-04	1.1060E-04

Table 4.3 Constant-volume Explosion: Final state - Nobel-Abel EOS

	Theory	Model
Temperature (K)	1875.2	1875.2
Pressure (atm)	2302.4	2302.4
Mass % -H2	8.7004E-08	8.6994E-08
Mass % - O2	1.2697E-01	1.2697E-01
Mass % - N2	7.5705E-01	7.5705E-01
Mass % - H2O	1.1587E-01	1.1587E-01
Mass % - OH	1.1060E-04	1.1060E-04

Table 4.4 Constant-volume Explosion: Final state - van der Waals EOS

	Theory	Model
Temperature (K)	1896.8	1896.8
Pressure (atm)	3001.1	3001.1
Mass % -H2	5.2517E-08	5.2535E-08
Mass % - O2	1.2697E-01	1.2697E-01
Mass % - N2	7.5705E-01	7.5705E-01
Mass % - H2O	1.1587E-01	1.1588E-01
Mass % - OH	1.1003E-04	1.1003E-04

Table 4.5 Constant-volume Explosion: Final state - Redlich-Kwong EOS

	Theory	Model
Temperature (K)	1864.9	1864.9
Pressure (atm)	2702.5	2702.5
Mass % -H2	5.3548E-08	5.3137E-08
Mass % - O2	1.2697E-01	1.2697E-01
Mass % - N2	7.5705E-01	7.5705E-01
Mass % - H2O	1.1588E-01	1.1588E-01
Mass % - OH	9.5393E-05	9.5399E-05

4.4 Test Case 3 - Isentropic Venting

In order to isolate a test case on the nozzle outflow source term, a case was run to compare the HGI simulation against theory for an isentropic discharge of a thermally perfect gas through a sonic nozzle. Here, the ideal solution assumes that the gas contained within the high-pressure chamber maintains spatially uniform pressure as the gas discharges. That is, it is assumed that pressure disturbances created by the outflow of gas travel at an infinite speed of sound and therefore the chamber pressure equilibrates instantaneously. Given these assumptions, the analytic solution for the isentropic blow-down was calculated using (Saad, 1993):

$$t = \frac{-1}{C} \frac{2\gamma}{1-\gamma} \left(p_f^{(1-\gamma)/2\gamma} - p_i^{(1-\gamma)/2\gamma} \right) \tag{4.1}$$

where:

$$C = \frac{\gamma}{V} \frac{R\sqrt{T_i}A}{p_i^{(\gamma-1)/2\gamma}} \sqrt{\frac{\gamma}{R} \left(\frac{2}{\gamma+1} \right)^{(\gamma+1)/(\gamma-1)}} \tag{4.2}$$

Equations (4.1) and (4.2) assume constant specific heat ratio. The HGI numerical solution calculates the specific heats as a function of temperature. Therefore, argon is used so that the specific heat ratio is constant for both solutions. The 241.8cc chamber is filled to an initial pressure of 10 atm and an initial temperature of 1,000 K. For the first case the grid in the numerical solution is reduced to (1 x 1) in order to neglect wave effects. The results from this initial test can be seen in Fig. 4.8. The graph shows that the code, using the method described in Section 2.3, produces results that are very close to the analytical case.

Next, to include wave effects, the same test was performed with a more realistic one-dimensional grid. The source term for the nozzle outflow was located in the first

computational cell on the left side of the inflator's chamber. The results from four cases

that use progressively finer meshes can be seen in Fig. 4.9. It is clear from the results that

there is a significant effect on the results due to the wave action. The solution oscillates

around the analytical result as the pressure wave, formed by the initial pressure drop in

the venting cell, moves along the length of the tube. The numerical solution does seem to

under-predict the time to vent all of the gas when compared to the analytical result. This

is due to a pressure and temperature drop that occurs near the nozzle. As the temperature

drops, the speed of sound at the nozzle decreases and the density increases. Both of these

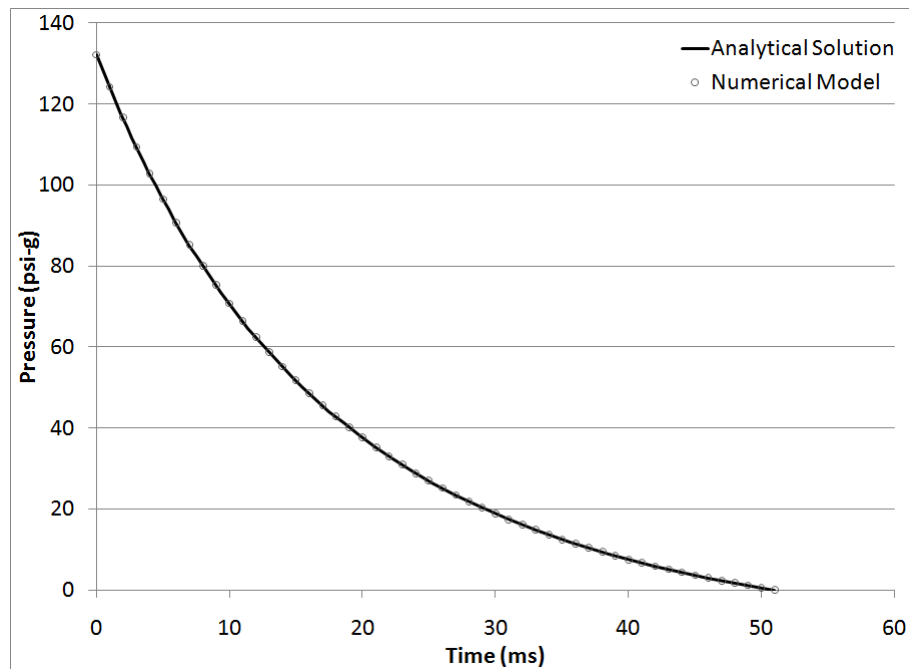have an effect on the nozzle outflow, explaining the difference in the solution.

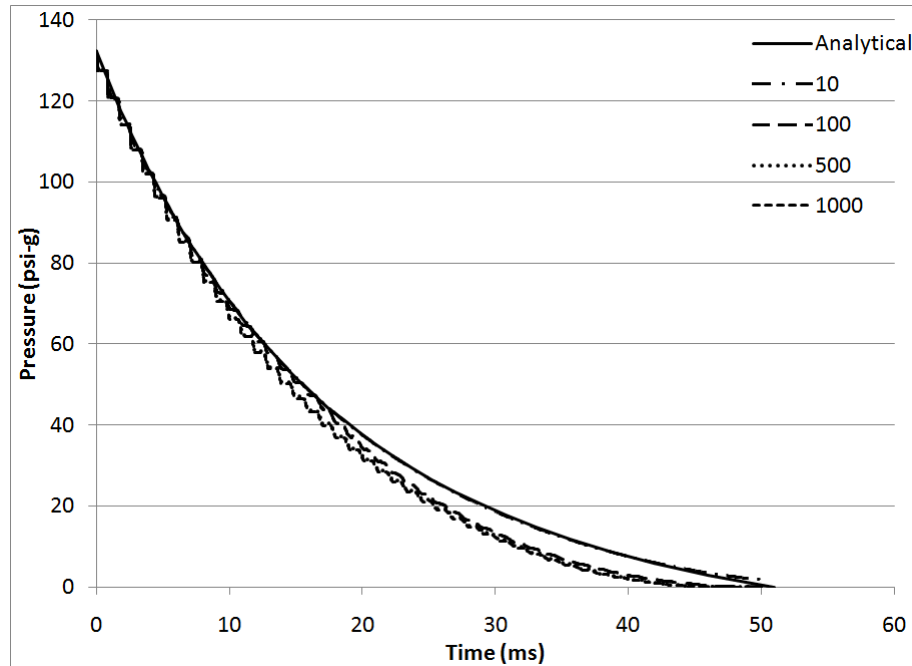Figure 4.8 Isentropic Discharge: Volume-averaged pressure decay.

Figure 4.9 Isentropic venting: Pressure profiles assuming 1D continuum

4.5 Test Case 4 - Detonation

The final validation cases run for the HGI code is a test of its ability to reproduce the characteristic features of a theoretical, steady-state detonation wave. Since the HGI conservation equations derived in Chapter 2 are cast in the generalized transient form, this implies that the solution to the HGI equations must demonstrate transition to a steady-state detonation propagating through space. This type of validation study provides a means to test the code's ability to converge on a theoretical, steady-state solution to a very complex shock-driven, supersonic reaction, starting from an initial non-detonation state. The process of transitioning from a slow burning, subsonic reaction wave to a supersonic detonation wave is referred to as Deflagration to Detonation Transition.

Detonation waves are driven by a non-reactive shock waves traveling through a reactive gas mixture. When the shock wave compresses the unburned gas, it causes an almost instantaneous increase in the temperature and pressure. If the fluid is assumed to be inviscid, the change in thermodynamic state is instantaneous. Moving in a reference frame travelling with the shock front, the "instantaneous increase" can be interpreted as a zero-thickness shock discontinuity. If the shock strength is large enough, this rapid increase in temperature can cause the gas following the wave to chemically react. This chemical reaction sustains the shock wave and propels it at supersonic speed relative to the oncoming fluid. The reaction zone is defined as the region from the state immediately behind the shock front to the location where the reaction is complete and the products of combustion are moving at the sonic velocity relative to the shock front. By definition, this state is referred to as the Chapman-Jouguet (CJ) point (Kuo, 1986) and the CJ properties are uniquely defined for a given reactive mixture. Knowing the initial state of a reactive mixture, CJ theory can be used to predict the speed at which the wave moves, D_{cj}, and the properties of the products (T_{cj}, P_{cj}, and composition). It should be noted that CJ theory does not predict anything about the structure of the reaction front. For that, one must solve the time evolving reaction equations. Thus, the challenge in this validation study is to reproduce both the correct CJ detonation properties as well as the approximate reaction zone thickness in HGI.

The initial conditions for the detonation test case are listed in Table 4.6. This represents a stoichiometric $H_2/O2$ mixture at elevated initial pressure and ambient temperature.

Table 4.6 Detonation wave test case initial conditions

Temperature (K)	300
Pressure (atm)	100
Mole % -H2	0.6667
Mole% - O2	0.3333

For the initial conditions given in Table 4.6, the steady state detonation wave properties

predicted by CJ theory are given in Table 4.7

Table 4.7 Theoretical CJ detonation state properties.

C-J STATE		
D	326553.5	(cm/s)
U	139086.5	(cm/s)
P-CJ	2197.8	(atm)
T-CJ	4683.69	(K)
RHO-mix	8.15E-02	[g/cc]

A high pressure reaction mechanism used by (Schmitt and Butler,1995a) was be

used in the HGI code to most accurately reproduce the theoretical results. This reaction

file is shown in Table 4.8.

Table 4.8 High Pressure, Hydrogen-Oxygen Reaction Mechanism

	REACTIONS			A_i	β_i	E_i
1	H+O2	=	OH+O	1.91E+14	0	1.64E+04
2	H2+O	=	H+OH	5.13E+04	2.67	6.29E+03
3	OH+H2	=	H+H2O	2.14E+08	1.51	3.43E+03
4	OH+OH	=	O+H2O	5.63E+11	0.31	1425
5	H2+M	=	H+H+M	8.51E+19	-1.1	1.04E+05
6	H+OH+M	=	H2O+M	1.38E+23	-2	0.00E+00
7	H+O2	=	HO2	4.79E+13	0	-384.8
8	H+HO2	=	OH+OH	1.70E+14	0	8.70E+02
9	H+HO2	=	H2+O2	6.61E+13	0	2.13E+03
10	HO2+O	=	O2+OH	1.74E+13	0	-399.1
11	OH+HO2	=	H2O+O2	1.45E+16	-1	0
12	H2O2+OH	=	H2O+HO2	1.75E+12	0	318
13	HO2+HO2	=	H2O2+O2	1.70E+13	0	4211.28

14	OH+OH	=	H2O2	7.59E+13	-0.37	0
15	H2O2+H	=	HO2+H2	4.79E+13	0	7.95E+03
16	H2O2+H	=	H2O+OH	1.00E+13	0	3.59E+03
17	O+H+M	=	OH+M	4.68E+18	-1	0
18	O+O+M	=	O2+M	3.98E+14	0	-1.79E+03
19	H2O2+O	=	OH+HO2	9.55E+06	2	3.97E+03

The reaction constants appearing in Table 4.8 are defined in Eq. (2.16), the expression for an Arrhenius forward reaction. In order to start the detonation wave in the HGI code, a small number of computational cells on the left side of the domain were initialized with the final properties of a constant volume explosion and a velocity of 3,000 m/s. In order to determine the appropriate grid size to accurately predict the CJ conditions, it was necessary to determine what the width of the reaction zone would be. Using Figure 4.10, found in Schmitt and Butler (1996), the approximate width of the combustion zone for an initial pressure of 100 atm was estimated to be around 5μm. Therefore, in order to accurately predict the results in HGI, the grid size would have to be less than 5μm. In order to reach such a small grid size and still maintain a reasonable total number of grid points and total computational time, the length of the domain was set to 2 cm. A series of cases was run in order to determine the appropriate grid size needed to properly resolve the combustion zone. These cases used grid sizes that varied from 20 μm to 0.5 μm. The best results for the CJ condition were found by locating the point where 95% of the reaction had been completed. The results from these runs can be seen below as Figs. 4.11 – 4.15.
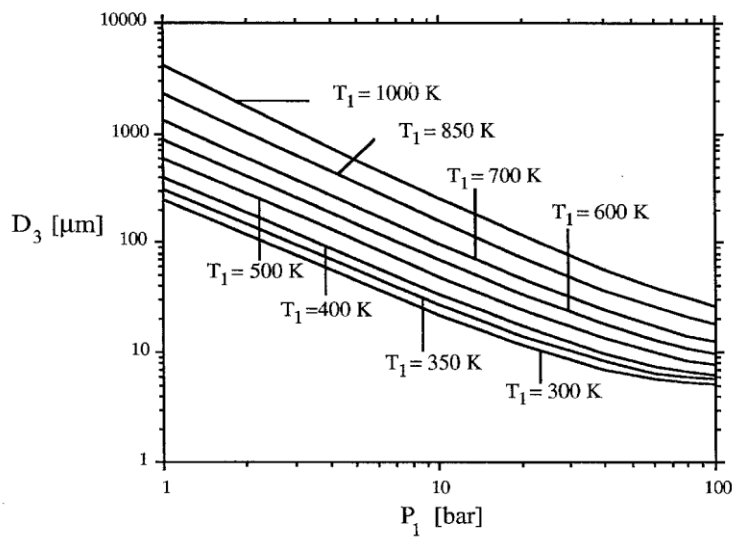
Figure 4.10 Reaction zone length as a function of initial pressure, taken from Schmitt (1994)
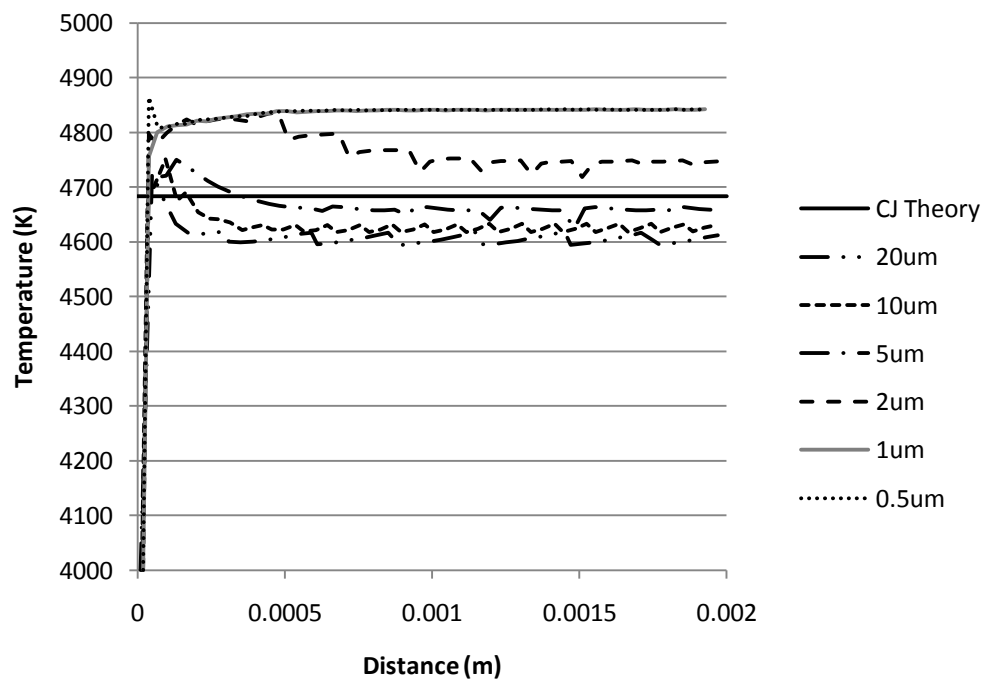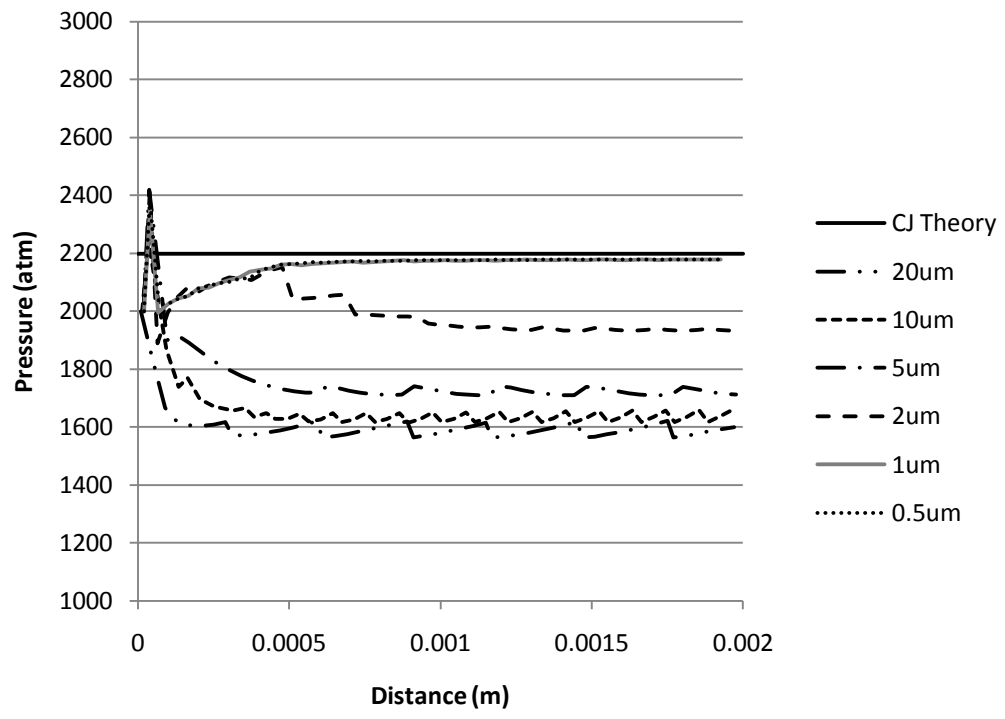

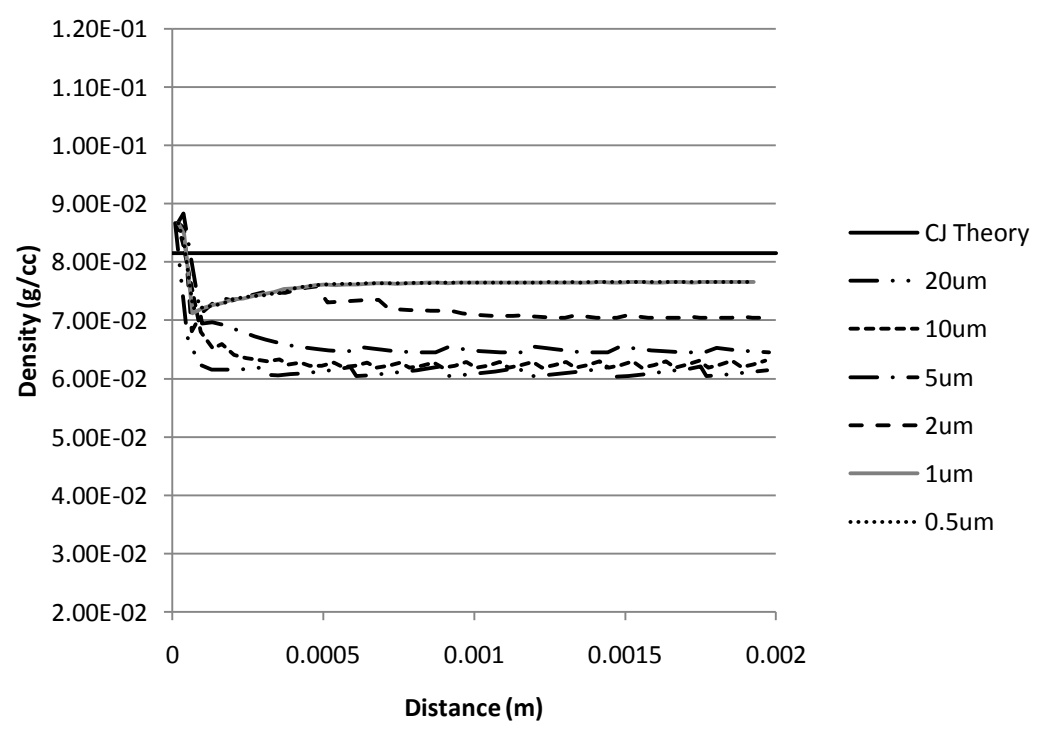Figure 4.11 CJ – Temperature (K)

Figure 4.12 CJ – Pressure (atm)
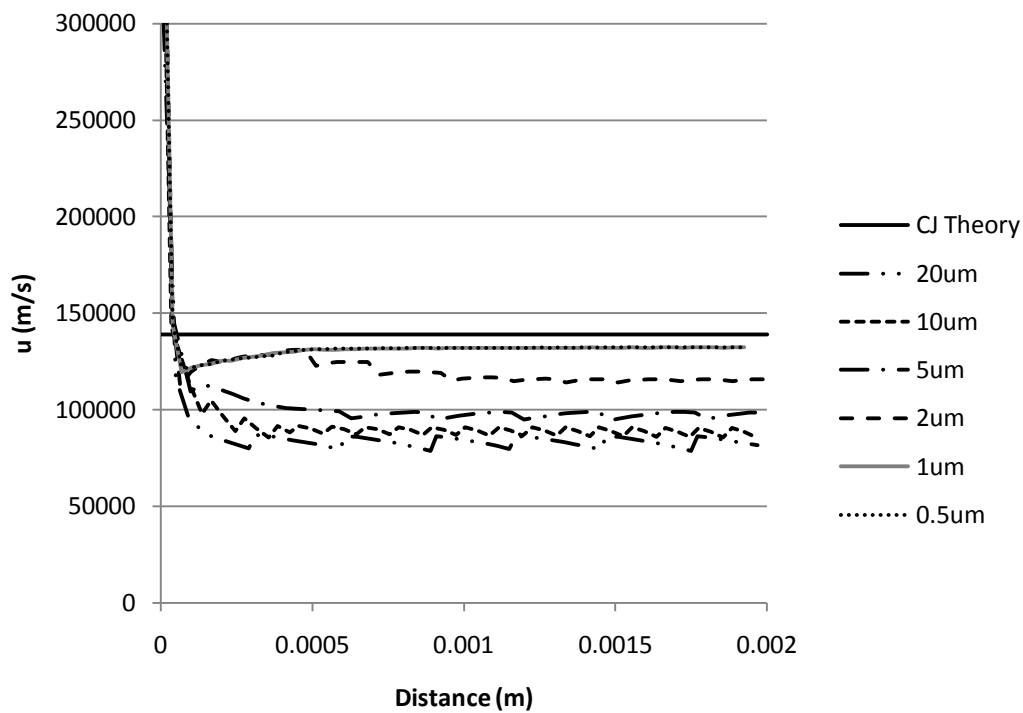

Figure 4.13 CJ – Density (g/cm^3)
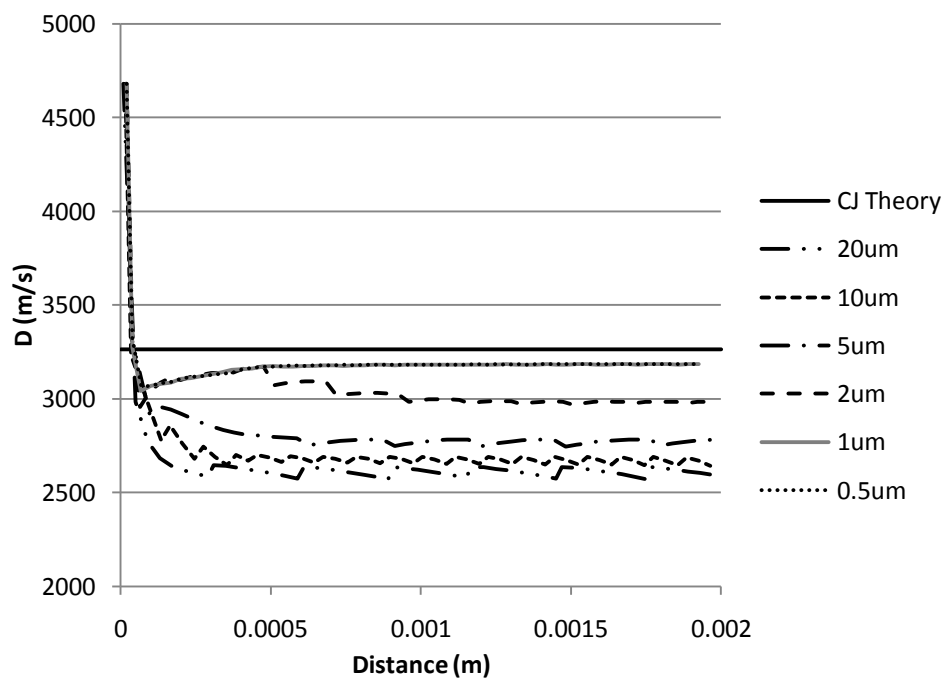
Figure 4.14 Gas velocity behind the wave (m/s)

Figure 4.15 Detonation wave velocity (m/s)

As demonstrated in Figs. 4.11 – 4.15, the solution for the detonation wave case changed until the grid size was reduced to less than the width of the combustion zone. This displays that in order to properly resolve the combustion zone which was around 5μm that there needed to be at least 5-10 points in the zone. Looking at Fig. 4.11, the temperature is higher than predicted by theory. Further investigation of the higher temperature showed that the majority of the reaction took place quickly inside the 5 μm combustion zone, but some of the reactions for the minor species continued far behind the reaction zone. This also explains why the results were best if taken when the reaction was 95% complete. If the reaction mechanism was modified to increase the speed of these minor reactions the results for the temperature should improve. The output for the rest of the variables examined was very close to the output predicted by theory. This proves the codes ability to predict the gas dynamics, handle large magnitude shock waves, and accurately calculate the appropriate heat release required to reach the theoretical detonation wave speed.

CHAPTER 5

RESULTS

5.1 Background – HGI State Calculations

Assembling an HGI requires precise control over the quantities of fuel, oxidizer, and air that are introduced into the inflator canister. This is necessary to ensure that the HGI has the prescribed initial state (pressure, density, chemical composition), and therefore functions exactly as designed. For example, a 1% error in the amount of hydrogen changes the stoichiometry enough to fail the prescribed performance specifications. Because of the extreme fill pressure of an HGI, the ideal gas assumption cannot be used to calculate state properties. Instead, it is necessary to use a real gas equation of state to reduce the error caused by neglecting the intermolecular forces that are more significant at high pressures and temperatures. In this chapter, state calculations are made using real gas equations of state that have been previously shown to represent the HGI non-ideal states. In all cases examined in this work, the inflator is filled with a 13% hydrogen (by volume) and 87% air mixture that is initially pressurized to approximately 42 MPa (6,000 psi).

Testing and qualification of an HGI is different from the actual in-vehicle functioning. When testing an HGI in the laboratory the inflator is placed in a rigid test chamber so that the properties of the combustion products can be recorded in a well-controlled environment. The difference between normal in-vehicle inflator operation and laboratory qualification testing is illustrated in Fig. 5.1. As illustrated in the figure, the volume of an airbag changes dramatically during deployment (top-half of Fig. 5.1). The volume initially increases due to the venting of the inflator, but then decreases as the
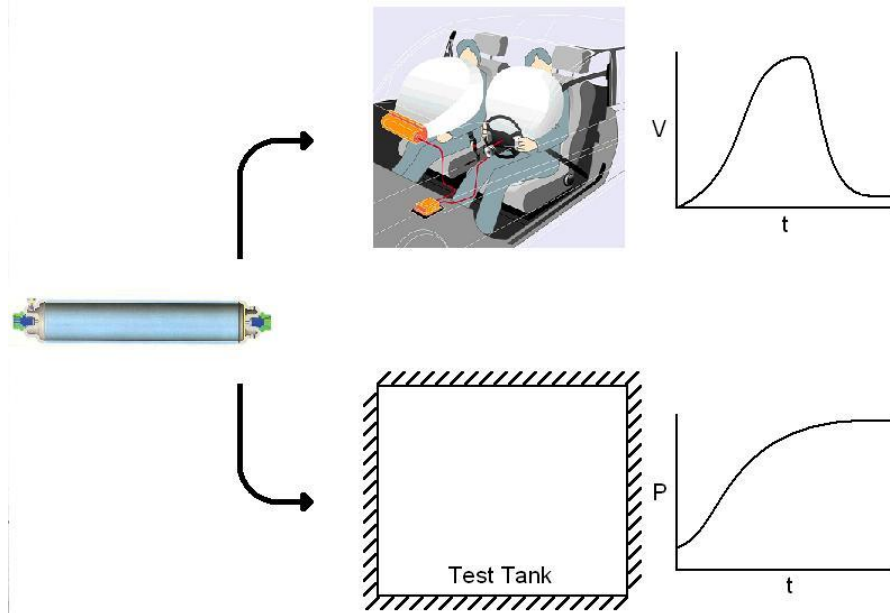
Figure 5.1 Illustration of HGI inflating vehicle airbags (top)
and typical constant-volume test apparatus (bottom).

occupant comes in contact with the bag. During this process, the bag maintains a

relatively constant pressure. For comparison, the standard "tank test" used for inflator

qualification is a process that fills a tank of constant volume (bottom-half of Fig. 5.1).

Therefore, as the products of combustion vent into the tank, the pressure increases. The

analysis performed herein will focus on the tank test. A number of relevant states during

the filling and deployment were chosen for the analysis. They are:

State A (Fig. 5.2): Inflator - Ambient conditions prior to filling.

State B (Fig. 5.3): Inflator – After hydrogen has been added.

State C (Fig. 5.4): Inflator – Immediately after Air/He has been added.

State D (Fig. 5.5): Inflator – After State C has thermally equilibrated with ambient

temperature (300 K)

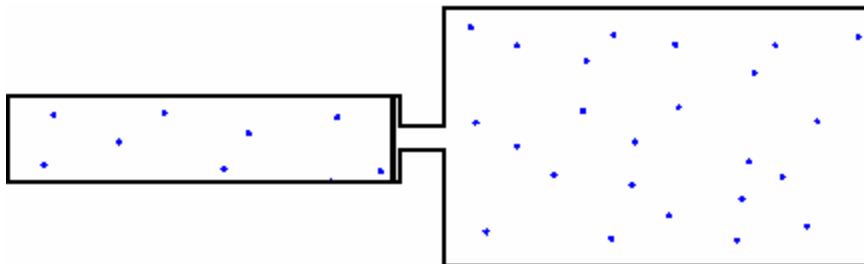State E (Fig. 5.6): Tank – Ambient conditions prior to inflator discharge.

Figure 5.2 State A – Ambient state before filling begins.
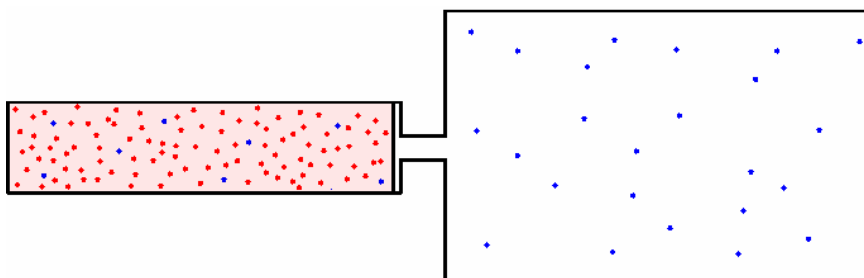

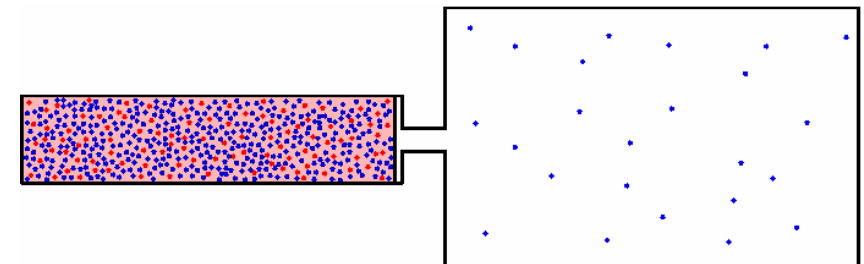Figure 5.3 State B - After hydrogen is added.

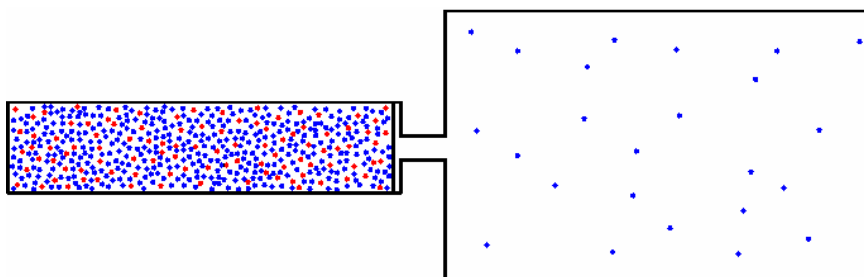Figure 5.4 State C - After Air-He is added.

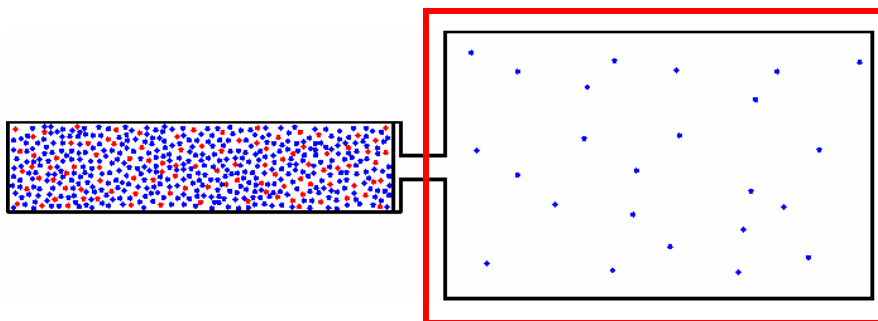Figure 5.5 State D - Completely filled inflator cooled to 300 K.

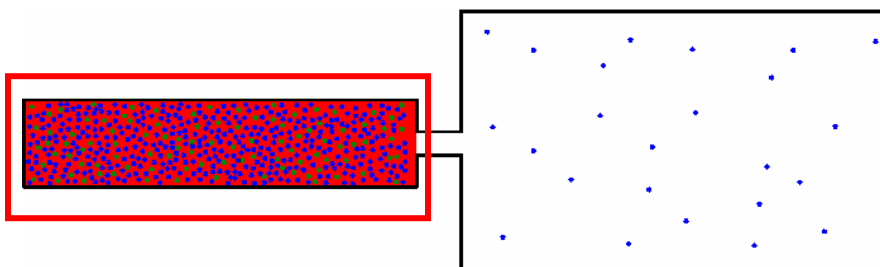Figure 5.6 State E – Initial state in tank at 300 K.

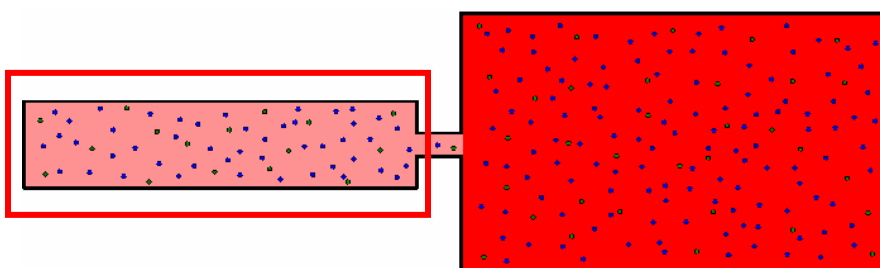Figure 5.7 State F - Inflator after combustion.
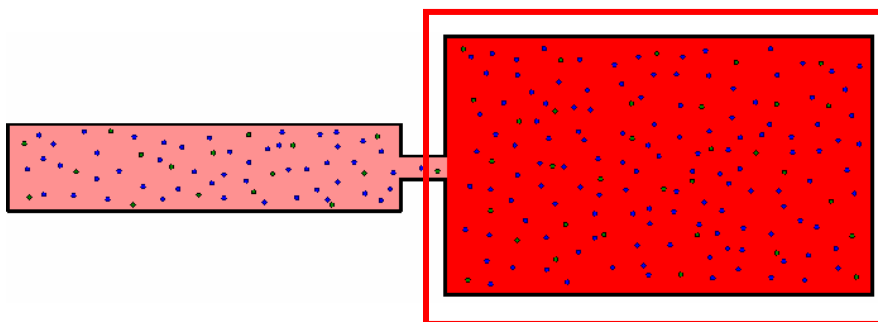

Figure 5.8 State G - Inflator after venting.

Figure 5. 9 State H - Tank after venting.

State F (Fig. 5.7): Inflator – After combustion, prior to discharge.

State G (Fig. 5.8): Inflator – After discharge to tank.

State H (Fig. 5.9): Tank – After inflator discharges into tank.

In Fig. 5.2, the ambient air that is present in the inflator and tank is represented by the blue particles. In Fig. 5.3, red dots are used to represent the hydrogen that was added to the system. The increase in pressure also causes an increase in the temperature in the inflator, which is represented by its pink background. In Fig. 5.4, the additional blue dots represent the additional air added to the system. The darker background shade of red represents the increase in temperature associated with the increase in mass and pressure. For a typical HGI the pressure at State D (after cooling to ambient temperature) is approximately 400 atm.

From the combustion of the hydrogen gas, the temperature and pressure in the inflator increase dramatically, reaching approximately 1,600 K and 2,000 atm (Fig. 5.7). In Fig. 5.7, the red dots, which previously represented hydrogen, have been replaced with green dots to represent the formation of water vapor. The color of the background in the inflator has changed to a bright red to represent the extremely high temperature and pressure in the inflator. The last two states that are calculated are the final states for the inflator (State G) and the tank (State H).

5.2 Results – HGI State Calculations

The mass of inflator gas at State D is a critical design target for HGIs and will be presented as the independent variable in the following discussion. For the calculations performed here, the volume of the canister is fixed at $V_i = 283.5$ cc, and the tank volume

is $V_t = 60$ L. In addition, the Redlich-Kwong form of the cubic equation of state was chosen for these calculations since it has been shown to accurately represent hydrogen-air mixtures at the states being considered. The analysis focuses on States D, G and H, where error in the pressure can affect energy-release and mass-flow rates.

Figure 5.10 displays the relationship between inflator gas mass and pressure at State D, illustrating how the error in the ideal gas model becomes non-negligible as initial pressure increases above 300 - 350 atm, typical minimum fill pressures for HGIs. Likewise, Fig. 5.11 illustrates the post-combustion, pre-discharge condition (State F). During discharge, sonic nozzle flow from the inflator to the tank is linearly dependent on the inflator pressure. If the pressure is calculated incorrectly, it will translate into an incorrect mass-flow rate.
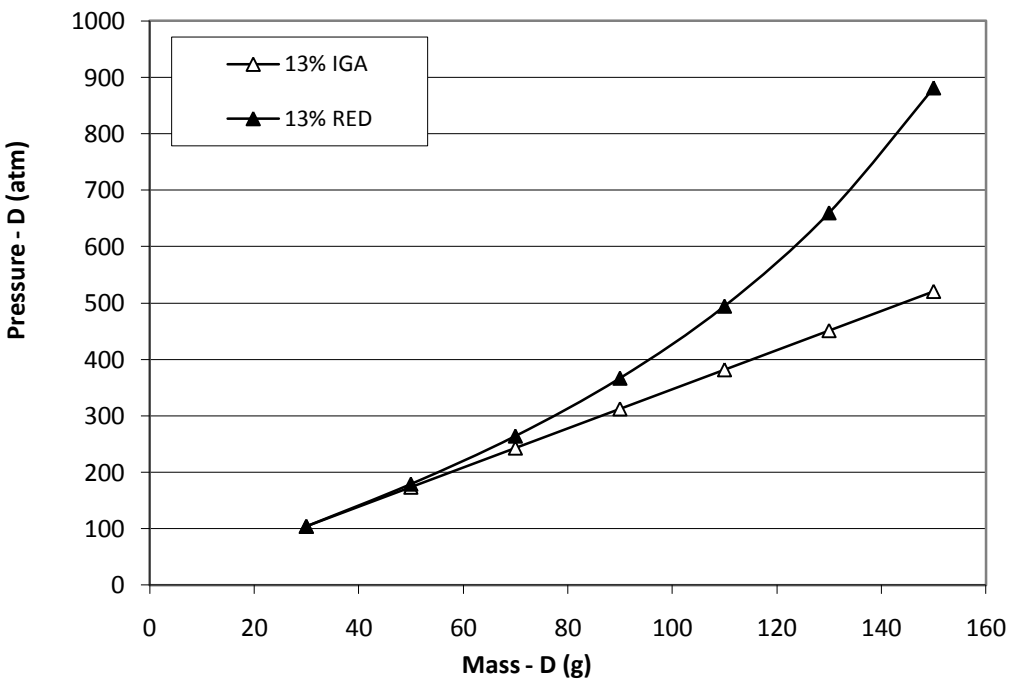
Figure 5.10 State D - Inflator pressure after cooling to ambient temperature calculated using Redlich-Kwong (RED) and Ideal Gas (IGA) equations of state.
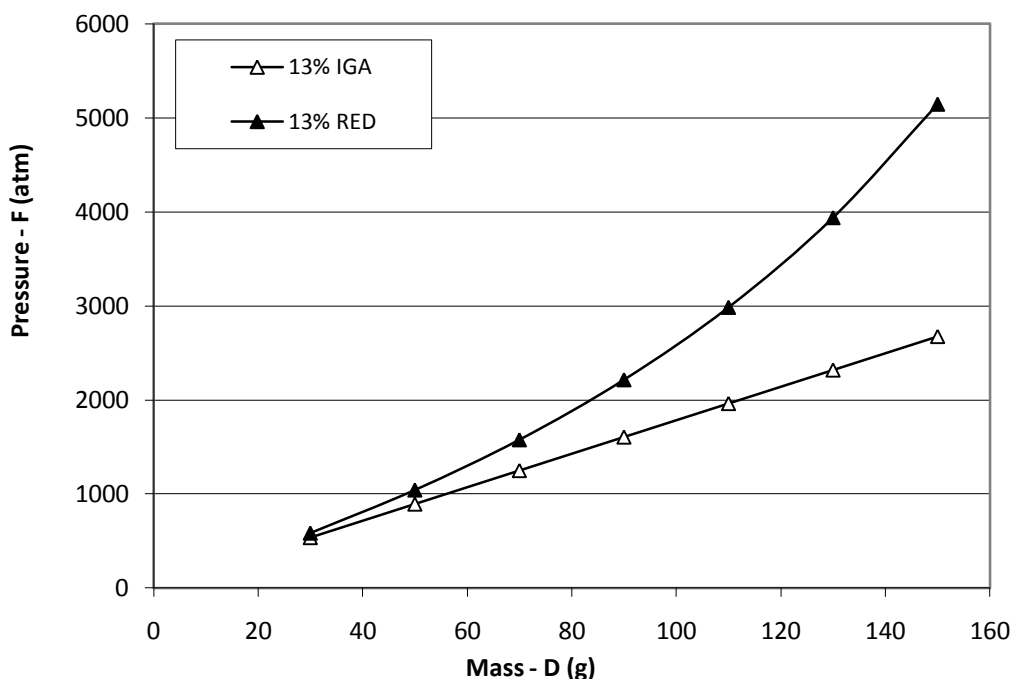
Figure 5.11 State F - Inflator pressure after combustion and before discharge.

Figures 5.12 and 5.13 illustrate how neglecting the compressibility factor throughout the process can affect the final tank state (State H), even though the compressibility factor at State H is close to 1.0. Finally, Table 5.1 displays the relative error involved with use of the ideal gas law relative to the real gas calculations made with the Redlich-Kwong equation of state. The highlighted row in Table 2 is representative of a common fill level in an HGI. When typical HGI cases were examined, it was found that many of the higher pressure states had approximately 20% error relative to the same case evaluated with the Redlich-Kwong Real Gas equation of state. Thus, it is suggested that a Real Gas equation of state be used when computing state properties for the current HGI designs.

Figure 5.12 State H - Tank pressure after inflator discharge.

Figure 5.13 State H - Tank temperature after discharge.

Table 5.1 Relative error between ideal gas and real gas equations of state for HGI.

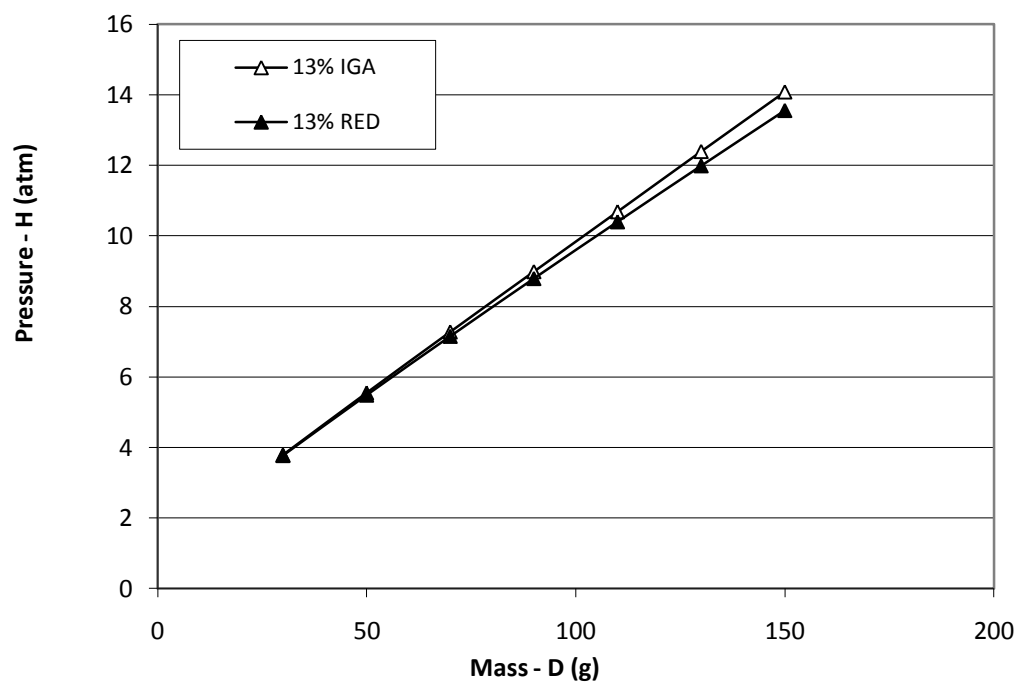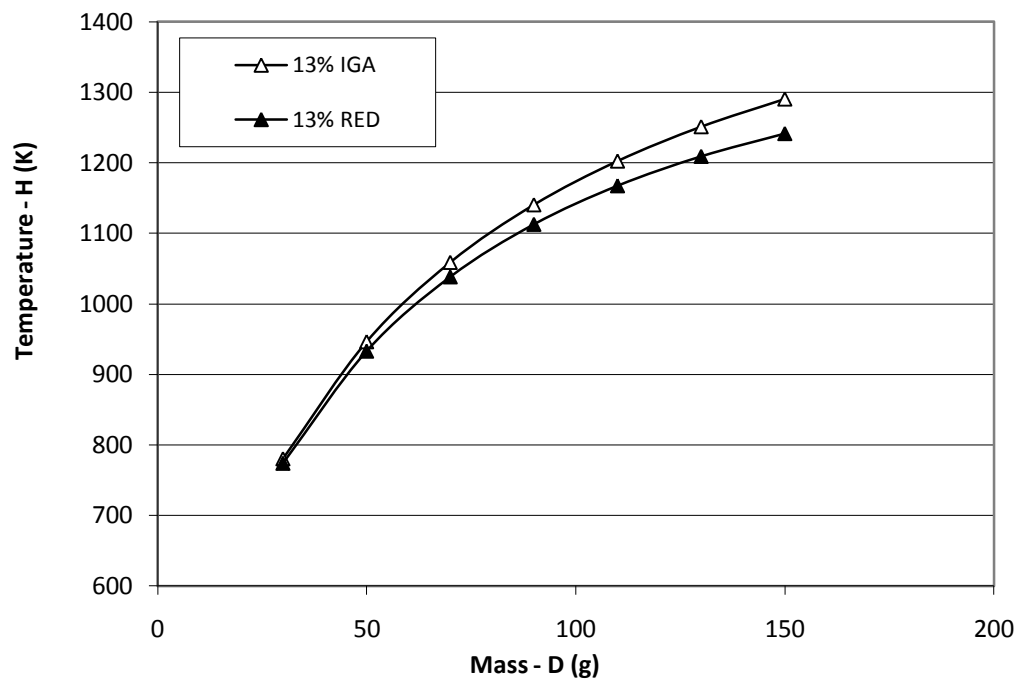| mass-D (g)	Pressure-D	Ti-G	Pi-G	Tf-G	Pf-G	Tf-H	Pf-H
30	0.48%	0.27%	8.43%	3.67%	0.64%	0.78%	0.64%
50	3.29%	0.43%	14.45%	6.45%	1.28%	1.39%	1.28%
70	8.16%	0.58%	20.81%	9.46%	1.96%	1.94%	1.82%
90	14.90%	0.72%	27.51%	12.80%	2.28%	2.45%	2.28%
110	22.82%	0.85%	34.26%	16.52%	2.79%	2.96%	2.79%
130	31.65%	0.98%	41.13%	20.76%	3.42%	3.44%	3.42%
150	40.92%	1.09%	48.00%	25.57%	3.91%	3.90%	3.91%

5.3 Results – HGI Transient Simulations

The previous section presented results for HGI state calculations using both the ideal gas and real gas equations of state. In this section, results are presented for HGI transient 1D simulations. The code has 2D capabilities, but since flow in the axial direction dominates and to decrease the run time of the simulation these initial test cases were performed using a 1D grid. Test cases are run using both the ideal gas and real gas equations of state. Again, the real gas equation of state that is used for all of the cases is the Redlich-Kwong. For both cases, the HGI combustion canister is initialized with the same initial mass, gaseous composition, and temperature. The volume of the bottle is 241.8 cc and the canister is 25cm in length. The cylinder has igniters on both ends, and for this test they will be triggered simultaneously. The ignition process is simulated by artificially raising the temperature for the species production equations in the first few centimeters on each end of the canister. To accomplish this, velocity and burn depth are

prescribed for both igniters. Using time and velocity, the position of the end of the igniter 'jet' is calculated. As the jet enters a new cell the temperature is increased in a linear fashion from just below the auto-ignition temperature of hydrogen to a value of 1,200 K. Once the jet has moved through a cell, the temperature remains at 1,200 K until the jet reaches the maximum burn depth. If the temperature of any of the cells in the ignition zone reaches a temperature above the ignition temperature calculated for the cell, the combustion subroutine is given the higher value. Once the jet reaches its prescribed burn depth the ignition is shut off and the combustion calculations return to using the actual cell temperature. It should be emphasized that this particular method of simulating the igniter reproduces the transient ignition process through a prescriptive algorithm, and is non-physical. Future models should incorporate a more physical-based ignition model.

In actual gas inflator tests the product gasses exit into a diffuser section and then into nozzles oriented in a radial fashion in order to produce no net force on the combustor (see, Fig. 1.4). The combustion chamber and the diffuser are separated by a burst disk that opens when the pressure inside the combustion chamber reaches a prescribed value. During a typical inflator ballistic cycle, the burst disk opens well before combustion of the canister gas is complete. In order to make the results of the test easier to examine, the simulation will be split into two parts: a combustion portion and a venting portion. In the combustion portion of this simulation the combustor burns completely. Then, after the combustion is complete, the vents open and the gas vents into a 60 L discharge tank. The prescribed time for the vents to open is $t = 20$ ms for all cases. The initial state for both cases is given in Table 5.2.

Table 5.2 HGI initial conditions

Initial Conditions	
Mass (g)	96.6
Temperature (K)	300
Mass % H2	15.83
Mass % O2	17.68
Mass % N2	66.49
Mass % H2O	0.000

The results from both the ideal gas and real gas simulations are shown in Figs.

5.14 – 5.17. Both cases use a reduced reaction chemical kinetics set created by the author.

This set was created due to the lack of reliable reaction sets developed for pressures as

high as 400 atm. This was done using a known characteristic burn time, for this style of

inflator, of around 10 ms. Since the grid size necessary to run this test would be affected

by the reaction file (i.e. the width of the reaction zone is affected by the reaction

mechanism), a grid size slightly smaller than that used in the shock tube validation test is

used. A grid of 1,600 cells was selected to discretize the 25 cm tube, which produces to a

grid size of 156.25 μm. Using the reaction set it was found that the reaction zone was

around 1 cm. This means that there are approximately 64 grid points within the reaction

zone at any time. Given the number of cells in the combustion zone and that the grid is

much smaller than necessary to accurately predict the gas dynamics, a grid analysis was

not performed. Given that the main goal of this analysis is to compare the use of ideal and

real gas equations of state and not to compare against actual test runs, it is believed that

this is a reasonable assumption.
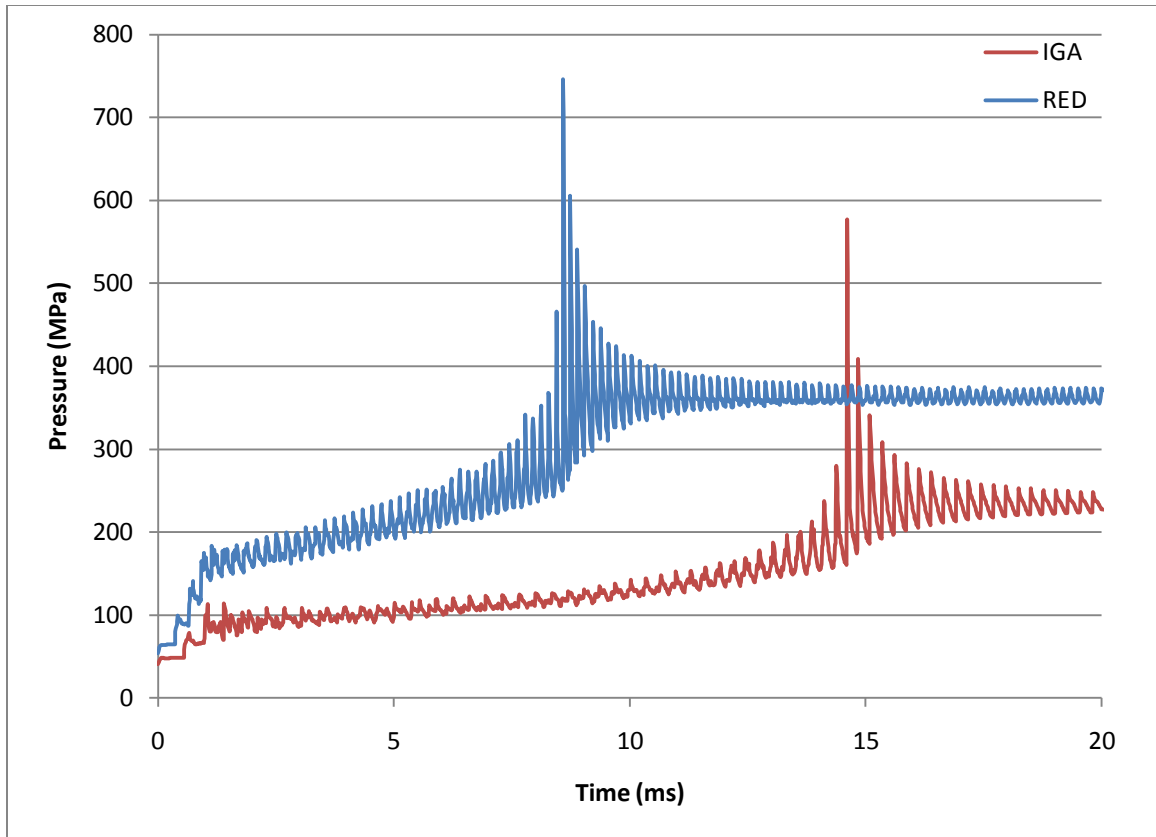
Figure 5.14 HGI Pressure at nozzle end of the inflator.

Figure 5.14 displays results for the two cases considered. The first feature to notice is the initial inflator pressure. Given that the specified initial conditions maintain the mass and temperature of the gas inside the inflator constant, a different initial pressure is calculated for each equation of state. After 1 ms the ignition process is complete and the gas begins to deflagrate from the igniters towards the centerline. The combustion continues until each run reaches its peak pressure. For the ideal gas and real gas equations of state this time is 14.5 ms and 8.54 ms, respectively. Peak pressures for both of the cases differ as well. The ideal case reaches a maximum pressure at the diffuser end just above 5,440 atm (80,000 psi), where the real gas case reaches a maximum pressure of around 7,480 atm (110,000 psi).

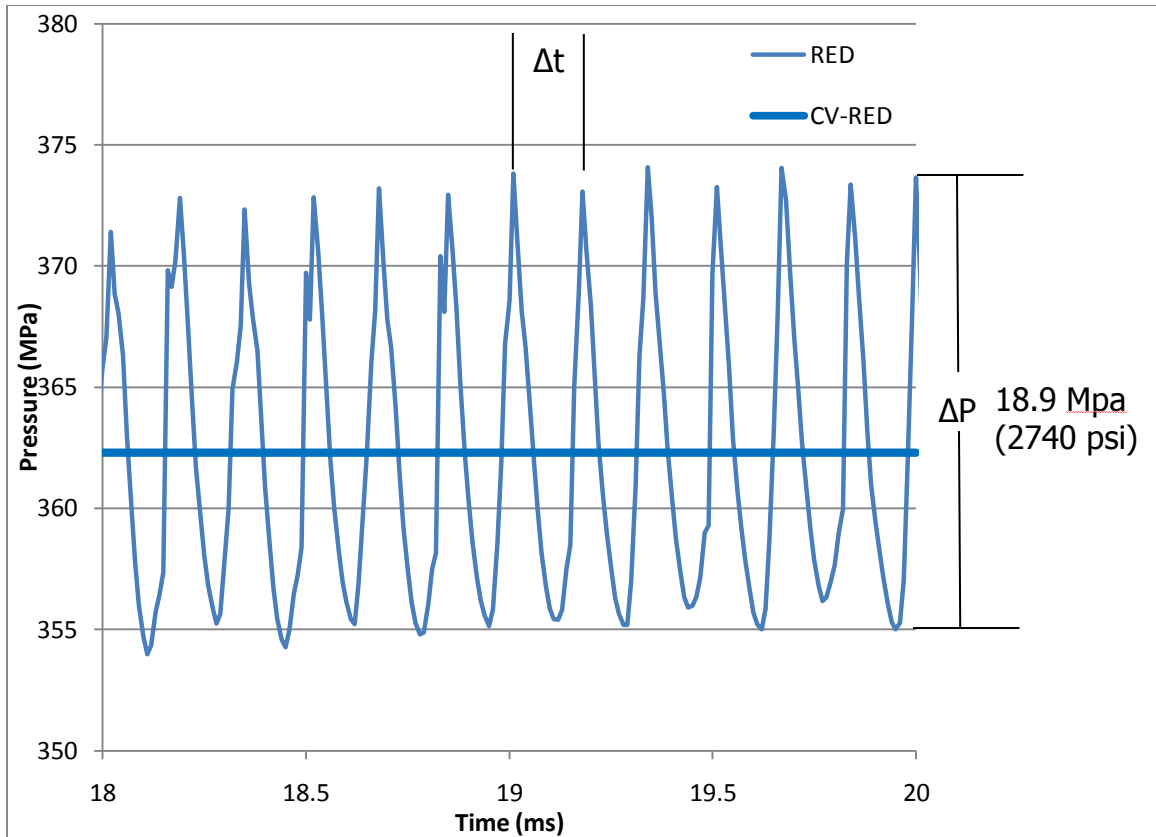Figure 5.15 HGI Combustor pressure at the nozzle end of inflator, Redlich-Kwong EOS, enlarged view of pressure oscillations before venting, 18-20 ms

Another obvious feature for both cases is the longitudinal pressure oscillations in the inflator. After combustion is terminated, and before the nozzles open at 20ms, the frequencies of the oscillations in both cases become very clear. It is clear that the real gas case has a much higher frequency that that of the ideal case. Closer measurement of the data reveals that the average period of each pressure cycle is around 0.1656 ms (6,036 Hz) for the real gas case and 0.2636 ms (3,794 Hz) for the ideal gas case. The wave for each of these cycles is traveling 12.5 cm from the igniter to the middle of the canister where, due to the symmetry of the dual ignitor setup, the wave is reflected back and travels another 12.5cm for a total distance of 25 cm. Using this distance and the periods of both of the waveforms (Δt), the nominal wave speed is calculated to be 948 and 1,509

m/s for the real and ideal cases, respectively. These are close to the speed of sounds of 863 and 1371 m/s predicted by theory. Figure 5.15 displays that the magnitude of the pressure oscillations for the Redlich-Kwong EOS after combustion, is around 18.9 MPa (2740 psi). These destructive pressure waves fluctuate around the constant volume final pressure of 362 MPa (52527 psi) predicted by theory.

The next stage of the simulation examines how the gas assumption affects the gas discharge into the 60 L test tank. Figure 5.16 demonstrates that the final inflator pressure (i.e., pre-discharge) for the real gas case is much higher than that of the ideal gas case. These profiles are for the nozzle end of the inflator. This difference in pressure causes the nozzle outflow for the real case to be much higher than that of the ideal case. This is because sonic nozzle flow is linearly dependent on the inflator pressure as shown in Eq. (2.19). This higher outflow results in a faster increase in tank pressure during the first few milliseconds of discharge. Accurately predicting the discharge tank pressure-rise rate is important since it is one of the design specifications controlled by Federal requirements. On the contrary, Fig. 5.17 shows that there is little difference in the predicted final tank pressure.
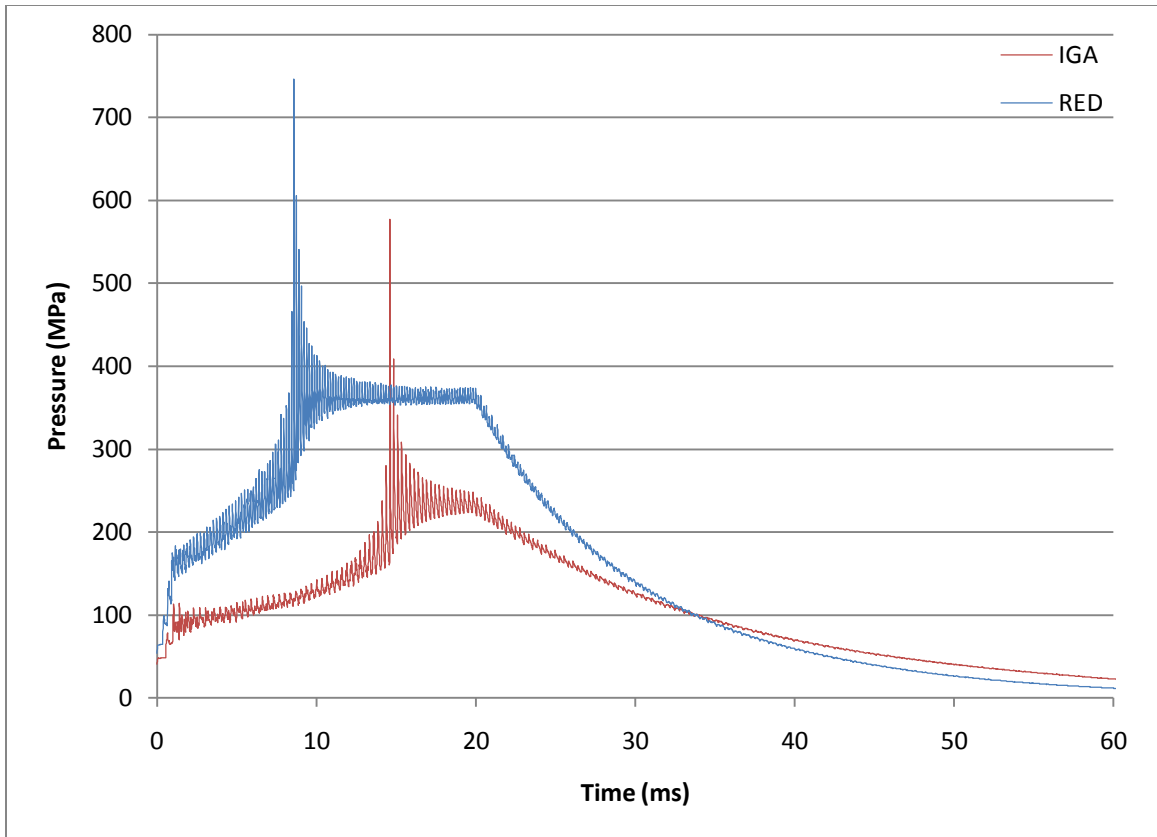
Figure 5.16 HGI Combustor pressure at the nozzle end of inflator, with venting
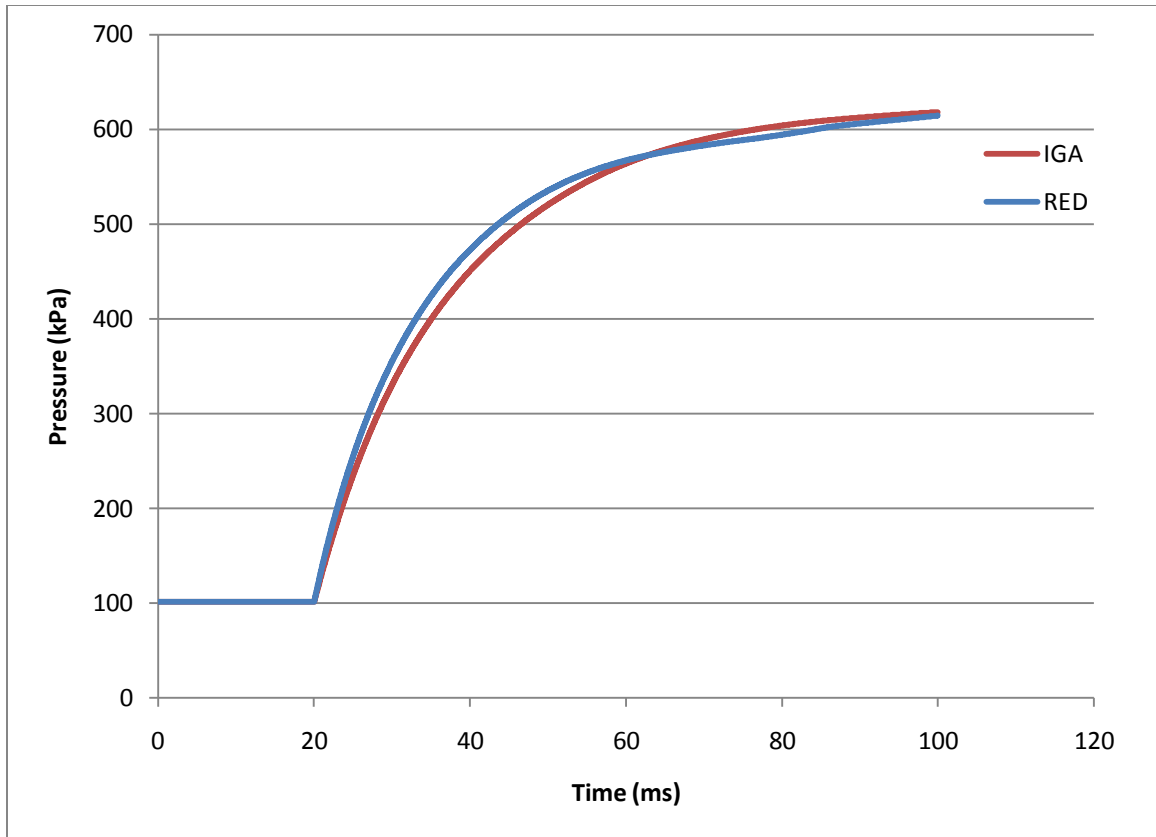
Figure 5.17 Pressure data for the 60L test tank

Since many of these key design parameters are greatly affected by the type of gas assumption used, it is clear why the use of the more accurate real gas assumption is necessary. For example, if the combustor is designed using the ideal gas assumption the higher peak pressure predicted by the real gas equation of state means that it is possible that the combustor bottle could unexpectedly rupture during operation. The total time taken to react and vent the products is a very important design parameter for an automotive airbag inflator. If this time is overestimated by assuming ideal gas the inflator may perform outside of its design constraints.

CHAPTER 6

CONCLUSIONS AND RECOMMENDATIONS

In order to properly model the wave dynamics seen in Heated Gas Inflators, a CFD model was added to an existing Airbag Inflator Model capable of performing real gas equation of state calculations. A high resolution shock capturing technique was used in order to handle the sharp discontinuities from pressure waves and in the species equations at the combustion front. The code was validated using well-documented tests with known analytical or theoretical solutions. The error associated with using the ideal gas assumption for volume averaged state calculations was quantified in Table 5.1. To determine the effect the equation of state has on the final state properties, combustion, wave dynamics, and nozzle outflow, two test cases were run using both the ideal gas assumption and the Redlich-Kwong real gas equation of state. From these test cases it was determined that the need for real gas equations of state was significant. The chosen equation of state had a considerable effect on key design parameters such as the initial pressure, flame propagation, peak combustor pressures, and mass flow rate into the test tank. The total combustion time for the ideal gas case was over 40% slower than that of the real gas simulation. The peak pressure in the combustor was much higher for the real gas case, around 38% higher than that calculated using ideal gas. When comparing the mass flow at the output nozzle it was found that the real gas case, due to its higher pressure, had a much higher flow rate than that of the ideal case, resulting in a faster rise in pressure in the 60 L test tank. These are just some of the key design parameters that are affected by the state calculations inside the combustion chamber. If ideal gas is assumed

at these high pressures not only will the calculations for the design parameters be incorrect, the performance of this safety device could be compromised.

In the future, the Airbag Inflator Model can be used to determine the effects of other design parameters such as ignition delay times or the outcome of using different gas compositions. Other parameters such different initial temperatures, found in extremely hot or cold environments, have been known to cause significant effects on inflator performance. The studies performed in this analysis were done in one dimension. Further investigations could be done using the codes already existing 2D axisymmetric capabilities to more accurately model the inflator process. Implementing the 2D abilities allows the use of more realistic nozzle outflow calculations and ignition methods. One common ignition method that could be used is to inject very hot nonreactive gas at the center cells on each end of the cylinder. This would more closely simulate the hot products that are shot into the inflator by the ignitors.

More investigation should be done on finding an accurate way of simulating the chemical kinetics at these high pressures. Once an accurate reaction mechanism is developed, a grid analysis should be performed to determine the appropriate grid size for the new reaction mechanism. Once this is done, the model could be compared to actual inflator experimental data. After the simulations accurately reproduce the results from the experimental data, the code could be used for initial design modifications. This could reduce the number of prototypes that need to be manufactured and tested, reducing the total cost of the inflator design.

APPENDIX A

NUMERICAL SOLUTION METHOD

A.1 Time Splitting Method

$$\frac{\partial U}{\partial t} + \frac{\partial F(U)}{\partial x} + \frac{\partial G(U)}{\partial y} = S(U) \tag{A.1}$$

$$\frac{\partial U}{\partial t} + \frac{\partial F(U)}{\partial x} + \frac{\partial G(U)}{\partial y} = 0 \tag{A.2}$$

Initial conditions $U(x,y,t^n) = U^n$ \hfill (A.3)

$$\frac{\partial U}{\partial t} = S(U) \tag{A.4}$$

Initial conditions: $U(x,y,t^n) = \overline{U}$ \hfill (A.5)

$$U^{n+1} = S^{(\Delta t)}C^{(\Delta t)}(U^n) \tag{A.6}$$

$$U^{n+1} = C^{(\Delta t/2)}S^{(\Delta t)}C^{(\Delta t/2)}(U^n) \tag{A.7}$$

A.2 Flux Vector Splitting

$$\frac{\partial F}{\partial x} = \frac{\partial F}{\partial U}\frac{\partial U}{\partial x} = A(U)\frac{\partial U}{\partial x}, \quad \frac{\partial G}{\partial y} = \frac{\partial G}{\partial U}\frac{\partial U}{\partial y} = B(U)\frac{\partial U}{\partial y} \tag{A.8}$$

$$F = A(U)U, \quad G = B(U)U \tag{A.9}$$

$$U = \begin{bmatrix} \rho \\ \rho u \\ \rho v \\ E \\ \rho Y_k \end{bmatrix} = \begin{bmatrix} u_1 \\ u_2 \\ u_3 \\ u_4 \\ u_5 \end{bmatrix}, \quad F(U) = \begin{bmatrix} \rho u \\ \rho u^2 + P \\ \rho uv \\ u(E + P) \\ \rho u Y_k \end{bmatrix} = \begin{bmatrix} f_1 \\ f_2 \\ f_3 \\ f_4 \\ f_5 \end{bmatrix} \tag{A.10}$$

$$A(U) = \frac{\partial F}{\partial U} = \begin{bmatrix} \partial f_1/\partial u_1 & \partial f_1/\partial u_2 & . & . & \partial f_1/\partial u_5 \\ \partial f_2/\partial u_1 & . & . & . & . \\ . & . & . & . & . \\ . & . & . & . & . \\ \partial f_5/\partial u_1 & . & . & . & \partial f_5/\partial u_5 \end{bmatrix} \tag{A.11}$$

$$A = \begin{bmatrix} 0 & 1 & 0 & 0 & 0 \\ a^2 - u^2 - \Phi P_e / \rho & 2u - u P_e / \rho & -v P_e / \rho & P_e / \rho & 0 \\ -uv & v & u & 0 & 0 \\ -uH - ua^2 - u\Phi P_e / \rho & H - u^2 P_e / \rho & -uv P_e / \rho & u + u P_e / \rho & 0 \\ -u Y_k & Y_k & 0 & 0 & u \end{bmatrix} \qquad (A.12)$$

$$H = \frac{E + P}{\rho} \qquad (A.13)$$

$$q = u^2 + v^2, \quad \Phi = H - q \qquad (A.14)$$

$$G(U) = \begin{bmatrix} \rho v \\ \rho uv \\ \rho v^2 + P \\ v(E + P) \\ \rho v Y_k \end{bmatrix} = \begin{bmatrix} g_1 \\ g_2 \\ g_3 \\ g_4 \\ g_5 \end{bmatrix} \qquad (A.15)$$

$$B(U) = \frac{\partial G}{\partial U} = \begin{bmatrix} \partial g_1 / \partial u_1 & \partial g_1 / \partial u_2 & . & . & \partial g_1 / \partial u_5 \\ \partial g_2 / \partial u_1 & . & . & . & . \\ . & . & . & . & . \\ . & . & . & . & . \\ \partial g_5 / \partial u_1 & . & . & . & \partial g_5 / \partial u_5 \end{bmatrix} \qquad (A.16)$$

$$B = \begin{bmatrix} 0 & 1 & 0 & 0 & 0 \\ -uv & v & u & 0 & 0 \\ a^2 - u^2 - \Phi P_e / \rho & 2u - u P_e / \rho & -v P_e / \rho & P_e / \rho & 0 \\ -vH - va^2 - v\Phi P_e / \rho & -uv P_e / \rho & H - v^2 P_e / \rho & v + v P_e / \rho & 0 \\ -v Y_k & 0 & Y_k & 0 & v \end{bmatrix} \qquad (A.17)$$

$$\left| A - \lambda_A I \right| = 0, \quad \left| B - \lambda_B I \right| = 0 \qquad (A.18)$$

$$\lambda_A = u - a, u, u, u, u + a \qquad (A.19)$$

$$\lambda_B = v - a, v, v, v, v + a \qquad (A.20)$$

$$a = \sqrt{\gamma R T} \qquad (A.21)$$

$$K = \begin{bmatrix} 1 & 1 & 0 & 0 & 1 \\ u-a & u & 0 & 0 & u+a \\ v & v & 1 & 0 & v \\ H-ua & \frac{1}{2}(u^2+v^2) & v & 0 & H+ua \\ Y_k & 0 & 0 & 1 & Y_k \end{bmatrix} \tag{A.22}$$

$$L = \begin{bmatrix} 1 & 1 & 0 & 0 & 1 \\ u & u & 1 & 0 & u \\ v-a & v & 0 & 0 & v+a \\ H-va & \frac{1}{2}(u^2+v^2) & u & 0 & H+va \\ Y_k & 0 & 0 & 1 & Y_k \end{bmatrix} \tag{A.23}$$

Non-negative eigenvalues: $\lambda_{Ai}^+ = \frac{1}{2}\left[\lambda_{Ai} + |\lambda_{Ai}|\right]$ (A.24)

Non-positive eigenvalues: $\lambda_{Ai}^- = \frac{1}{2}\left[\lambda_{Ai} - |\lambda_{Ai}|\right]$ (A.25)

$$A = K\Lambda_A K^{-1} = K\Lambda_A^+ K^{-1} + K\Lambda_A^- K^{-1} = A^+ + A^- \tag{A.26}$$

$$F = AU = (A^+ + A^-)U = A^+U + A^-U = F^+ + F^- \tag{A.27}$$

$$F^\pm = \frac{\rho}{2\gamma} \begin{bmatrix} \lambda_{A1}^\pm + 2(\gamma-1)\lambda_{A2}^\pm + \lambda_{A3}^\pm \\ (u-a)\lambda_{A1}^\pm + 2(\gamma-1)u\lambda_{A2}^\pm + (u+a)\lambda_{A3}^\pm \\ v\lambda_{A1}^\pm + 2(\gamma-1)v\lambda_{A2}^\pm + v\lambda_{A3}^\pm \\ (H-ua)\lambda_{A1}^\pm + (\gamma-1)(u^2+v^2)\lambda_{A2}^\pm + (H+ua)\lambda_{A3}^\pm \\ Y_k\lambda_{A1}^\pm + 2(\gamma-1)Y_k\lambda_{A2}^\pm + Y_k\lambda_{A3}^\pm \end{bmatrix} \tag{A.28}$$

Non-negative eigenvalues: $\lambda_{Bi}^+ = \frac{1}{2}\left[\lambda_{Bi} + |\lambda_{Bi}|\right]$ (A.29)

Non-positive eigenvalues: $\lambda_{Bi}^- = \frac{1}{2}\left[\lambda_{Bi} - |\lambda_{Bi}|\right]$ (A.30)

$$B = L\Lambda_B L^{-1} = L\Lambda_B^+ L^{-1} + L\Lambda_B^- L^{-1} = B^+ + B^- \tag{A.31}$$

$$G = BU = (B^+ + B^-)U = B^+U + B^-U = G^+ + G^- \tag{A.32}$$

$$G^{\pm} = \frac{\rho}{2\gamma}\begin{bmatrix} \lambda_{B1}^{\pm} + 2(\gamma-1)\lambda_{B2}^{\pm} + \lambda_{B3}^{\pm} \\ u\lambda_{B1}^{\pm} + 2(\gamma-1)u\lambda_{B2}^{\pm} + u\lambda_{B3}^{\pm} \\ (v-a)\lambda_{B1}^{\pm} + 2(\gamma-1)v\lambda_{B2}^{\pm} + (v+a)\lambda_{B3}^{\pm} \\ (H-va)\lambda_{B1}^{\pm} + (\gamma-1)(u^2+v^2)\lambda_{B2}^{\pm} + (H+va)\lambda_{B3}^{\pm} \\ Y_k\lambda_{B1}^{\pm} + 2(\gamma-1)Y_k\lambda_{B2}^{\pm} + Y_k\lambda_{B3}^{\pm} \end{bmatrix} \tag{A.33}$$

$$\frac{\partial U}{\partial t} = \frac{1}{\Delta x}\left[F_{i-1/2,j}(U_{i-1/2,j}^{n}) - F_{i+1/2,j}(U_{i+1/2,j}^{n})\right] + $$
$$\frac{1}{\Delta y}\left[G_{i,j-1/2}(U_{i,j-1/2}^{n}) - G_{i,j+1/2}(U_{i,j+1/2}^{n})\right] \tag{A.34}$$

$$F_{i-1/2,j} = F_{i-1/2,j}^{+} + F_{i-1/2,j}^{-}, \qquad F_{i+1/2,j} = F_{i+1/2,j}^{+} + F_{i+1/2,j}^{-} \tag{A.35}$$

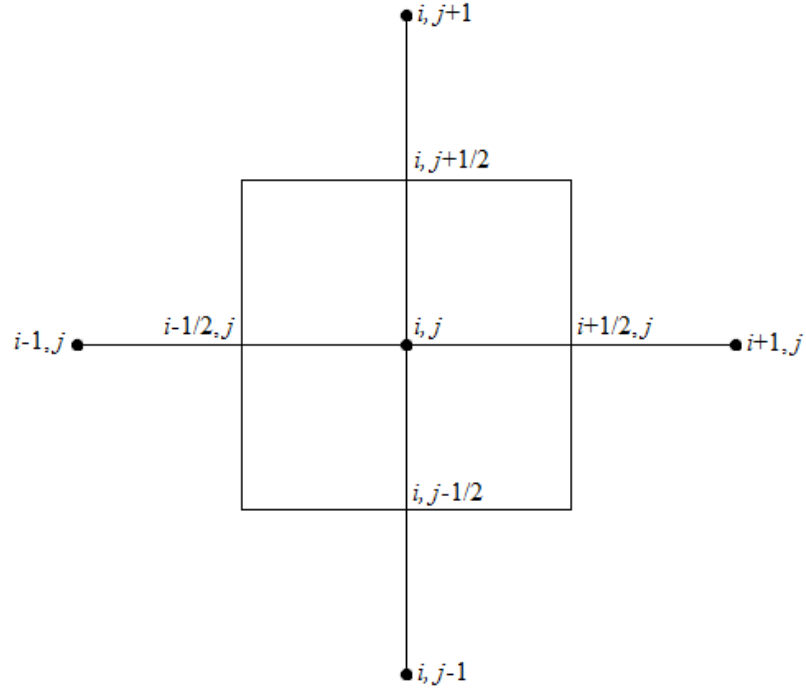$$G_{i,j-1/2} = G_{i,j-1/2}^{+} + G_{i,j-1/2}^{-}, \qquad G_{i,j+1/2} = G_{i,j+1/2}^{+} + G_{i,j+1/2}^{-} \tag{A.36}$$

Figure A.1 Cell interfaces in two dimensional space

$$F_{i+1/2,j}^{+} = F_{i,j}^{+} + \frac{1}{4}(1-\eta)\left[F_{i,j}^{+} - F_{i-1,j}^{+}\right] + \frac{1}{4}(1+\eta)\left[F_{i+1,j}^{+} - F_{i,j}^{+}\right] \tag{A.37}$$

$$F_{i+1/2,j}^{-} = F_{i+1,j}^{-} - \frac{1}{4}(1-\eta)\left[F_{i+2,j}^{-} - F_{i+1,j}^{-}\right] - \frac{1}{4}(1+\eta)\left[F_{i+1,j}^{-} - F_{i,j}^{-}\right] \tag{A.38}$$

$$F_{i-1/2,j}^{+} = F_{i-1,j}^{+} + \frac{1}{4}(1-\eta)\left[F_{i-1,j}^{+} - F_{i-2,j}^{+}\right] + \frac{1}{4}(1+\eta)\left[F_{i,j}^{+} - F_{i-1,j}^{+}\right] \tag{A.39}$$

$$F_{i-1/2,j}^{-} = F_{i,j}^{-} - \frac{1}{4}(1-\eta)\left[F_{i+1,j}^{-} - F_{i,j}^{-}\right] - \frac{1}{4}(1+\eta)\left[F_{i,j}^{-} - F_{i-1,j}^{-}\right] \tag{A.40}$$

$$F_{i-1/2,j}^{+} = F_{i-1,j}^{+} + \frac{1}{4}(1-\eta)\overline{\overline{\Delta}}_{i-3/2,j}^{+} + \frac{1}{4}(1+\eta)\overline{\Delta}_{i-1/2,j}^{+} \tag{A.41}$$

$$F_{i+1/2,j}^{+} = F_{i,j}^{+} + \frac{1}{4}(1-\eta)\overline{\overline{\Delta}}_{i-1/2,j}^{+} + \frac{1}{4}(1+\eta)\overline{\Delta}_{i+1/2,j}^{+} \tag{A.42}$$

$$F_{i-1/2,j}^{-} = F_{i,j}^{-} - \frac{1}{4}(1-\eta)\overline{\Delta}_{i+1/2,j}^{-} - \frac{1}{4}(1+\eta)\overline{\overline{\Delta}}_{i-1/2,j}^{-} \tag{A.43}$$

$$F_{i+1/2,j}^{-} = F_{i+1,j}^{-} - \frac{1}{4}(1-\eta)\overline{\Delta}_{i+3/2,j}^{-} - \frac{1}{4}(1+\eta)\overline{\overline{\Delta}}_{i+1/2,j}^{-} \tag{A.44}$$

$$G_{i,j-1/2}^{+} = G_{i,j-1}^{+} + \frac{1}{4}(1-\eta)\overline{\overline{\Delta}}_{i,j-3/2}^{+} + \frac{1}{4}(1+\eta)\overline{\Delta}_{i,j-1/2}^{+} \tag{A.45}$$

$$G_{i,j+1/2}^{+} = G_{i,j}^{+} + \frac{1}{4}(1-\eta)\overline{\overline{\Delta}}_{i,j-1/2}^{+} + \frac{1}{4}(1+\eta)\overline{\Delta}_{i,j+1/2}^{+} \tag{A.46}$$

$$G_{i,j-1/2}^{-} = G_{i,j}^{-} - \frac{1}{4}(1-\eta)\overline{\Delta}_{i,j+1/2}^{-} - \frac{1}{4}(1+\eta)\overline{\overline{\Delta}}_{i,j-1/2}^{-} \tag{A.47}$$

$$G_{i,j+1/2}^{-} = G_{i,j+1}^{-} - \frac{1}{4}(1-\eta)\overline{\Delta}_{i,j+3/2}^{-} - \frac{1}{4}(1+\eta)\overline{\overline{\Delta}}_{i,j+1/2}^{-} \tag{A.48}$$

$$\overline{\Delta}_{i+1/2,j}^{+} = Limiter(\Delta_{i+1/2,j}^{+}, \varpi\Delta_{i-1/2,j}^{+}) \tag{A.49}$$

$$\overline{\overline{\Delta}}_{i+1/2,j}^{+} = Limiter(\Delta_{i+1/2,j}^{+}, \varpi\Delta_{i+3/2,j}^{+}) \tag{A.50}$$

$$\overline{\Delta}_{i+1/2,j}^{-} = Limiter(\Delta_{i+1/2,j}^{-}, \varpi\Delta_{i-1/2,j}^{-}) \tag{A.51}$$

$$\overline{\overline{\Delta}}_{i+1/2,j}^{-} = Limiter(\Delta_{i+1/2,j}^{-}, \varpi\Delta_{i+3/2,j}^{-}) \tag{A.52}$$

$$\overline{\Delta}_{i,j+1/2}^{+} = Limiter(\Delta_{i,j+1/2}^{+}, \varpi\Delta_{i,j-1/2}^{+}) \tag{A.53}$$

$$\overline{\overline{\Delta}}_{i,j+1/2}^{+} = Limiter(\Delta_{i,j+1/2}^{+}, \varpi\Delta_{i,j+3/2}^{+}) \tag{A.54}$$

$$\overline{\Delta}_{i,j+1/2}^{-} = Limiter(\Delta_{i,j+1/2}^{-}, \varpi\Delta_{i,j-1/2}^{-}) \tag{A.55}$$

$$\overline{\overline{\Delta}}_{i,j+1/2}^{-} = Limiter(\Delta_{i,j+1/2}^{-}, \varpi\Delta_{i,j+3/2}^{-}) \tag{A.56}$$

$$\Delta_{i+1/2,j}^{+} = F_{i+1,j}^{+} - F_{i,j}^{+} \tag{A.57}$$

$$\Delta_{i+1/2,j}^{-} = F_{i+1,j}^{-} - F_{i,j}^{-} \tag{A.58}$$

$$\Delta_{i,j+1/2}^{+} = G_{i,j+1}^{+} - G_{i,j}^{+} \tag{A.59}$$

$$\Delta_{i,j+1/2}^{-} = G_{i,j+1}^{-} - G_{i,j}^{-} \tag{A.60}$$

$$\text{Minmod}(x, \varpi y) = \text{sgn}(x) . \max\{0, \min[|x|, \varpi\, y\, \text{sgn}(x)]\} \tag{A.61}$$

$$1 \le \varpi \le (3-\eta)/(1-\eta) \tag{A.62}$$

$$\begin{aligned}
\frac{\partial U}{\partial t} = \frac{1}{\Delta x}[&F_{i-1,j}^{+} + \frac{1}{4}(1-\eta)\overline{\overline{\Delta}}_{i-3/2,j}^{+} + \frac{1}{4}(1+\eta)\overline{\Delta}_{i-1/2,j}^{+} \\
&+ F_{i,j}^{-} - \frac{1}{4}(1-\eta)\overline{\Delta}_{i+1/2,j}^{-} - \frac{1}{4}(1+\eta)\overline{\overline{\Delta}}_{i-1/2,j}^{-} \\
&- F_{i,j}^{+} - \frac{1}{4}(1-\eta)\overline{\overline{\Delta}}_{i-3/2,j}^{+} - \frac{1}{4}(1+\eta)\overline{\Delta}_{i-1/2,j}^{+} \\
&- F_{i+1,j}^{-} + \frac{1}{4}(1-\eta)\overline{\Delta}_{i+3/2,j}^{-} + \frac{1}{4}(1+\eta)\overline{\overline{\Delta}}_{i+1/2,j}^{-}] \\
\frac{1}{\Delta y}[&G_{i,j-1}^{+} + \frac{1}{4}(1-\eta)\overline{\overline{\Delta}}_{i,j-3/2}^{+} + \frac{1}{4}(1+\eta)\overline{\Delta}_{i,j-1/2}^{+} \\
&+ G_{i,j}^{-} - \frac{1}{4}(1-\eta)\overline{\Delta}_{i,j+1/2}^{-} - \frac{1}{4}(1+\eta)\overline{\overline{\Delta}}_{i,j-1/2}^{-} \\
&- G_{i,j}^{+} - \frac{1}{4}(1-\eta)\overline{\overline{\Delta}}_{i,j-3/2}^{+} - \frac{1}{4}(1+\eta)\overline{\Delta}_{i,j-1/2}^{+} \\
&- G_{i,j+1}^{-} + \frac{1}{4}(1-\eta)\overline{\Delta}_{i,j+3/2}^{-} + \frac{1}{4}(1+\eta)\overline{\overline{\Delta}}_{i,j+1/2}^{-}]
\end{aligned} \tag{A.63}$$

APPENDIX B

SHOCK TUBE ANALYTICAL SOLUTION

B.1 Shock Tube Solution

The velocity of the shock is:

$$V_s = M_s c_1 = c_1 \left[\frac{\gamma_1 - 1}{2\gamma_1} + \frac{\gamma_1 + 1}{2\gamma_1} \frac{p_2}{p_1} \right]^{1/2}$$

(B.1)

The velocity of the gas in region 2 is:

$$V_2 = \left(\frac{c_1}{\gamma_1} \right) \left(\frac{p_2}{p_1} - 1 \right) \left[\frac{\frac{2\gamma_1}{\gamma_1 + 1}}{\frac{p_2}{p_1} + \frac{\gamma_1 - 1}{\gamma_1 + 1}} \right]^{1/2}$$

(B.2)

and:

$$V_3 = V_2$$

(B.3)

The density ratio across the shock is:

$$\frac{\rho_2}{\rho_1} = \frac{1 + \frac{\gamma_1 + 1}{\gamma_1 - 1} \frac{p_2}{p_1}}{\frac{\gamma_1 + 1}{\gamma_1 - 1} + \frac{p_2}{p_1}}$$

(B.4)

The temperature in region 3 is calculated using:

$$T_3 = T_4 \left(\frac{p_3}{p_4} \right)^{(\gamma_4 - 1)/\gamma_4}$$

(B.5)

where

$$p_3 = p_2$$

(B.6)

With T_3 known it is possible to calculate the c_3. The velocity of the tail wave in the

expansion region is:

$$V_{tail} = V_3 - c_3 \tag{B.7}$$

The velocity of the head wave in the expansion region is calculated as:

$$V_{head} = -c_4 \tag{B.8}$$

In order to determine the pressure curve in the expansion wave, the linear velocity profile was used to calculate the velocity at any point in the expansion wave. Knowing the velocity it is possible to calculate the pressure curve in the expansion region using:

$$p_{exp} = p_4 * \left(\left(1 - \frac{\gamma_4 - 1}{2} \right) \left(\frac{V_{exp}}{c_4} \right) \right)^{\frac{2\gamma_4}{\gamma_4 - 1}} \tag{B.9}$$

All other state calculations properties were found using the ideal gas equation of state.

REFERENCES

Anderson, John David. 1995. *Computational fluid dynamics: the basics with applications.* Mcgraw-Hill Series in Mechanical Engineering. New York: McGraw-Hill.

Bergan, N.E., "High-Pressure Thermodynamics in Combustion Processes," Ph.D Thesis, University of California at Davis, 1991.

Berger, J.M., and Butler, P.B., "Equilibrium Analysis of Three Classes of Automotive Airbag Inflator Propellants," *Combustion Science and Technology*, Vol. 104, No. 1-3, 1995, pp. 93-114.

Butler, P.B., Kang, J., and Krier, H., "Modeling and Numerical Simulation of the Internal Thermochemistry of an Automotive Airbag Inflator," Progress in Energy and Combustion Science, Vol. 19, 1993, pp. 365-382.

Butler, P. Barry, and Krier, Herman. 2000. Airbag inflator model user's guide. 4th ed. Combustion Sciences Inc.

Butler, P. Barry, and Schmitt , R.G. 1995. RGEQUIL. The University of Iowa.

Cannon, Jacob Eli. 2007. Thermal efficiency delivery of a detonation induced pulse jet. M.S. thesis, Department of Mechanical Engineering, The University of Iowa.

Hirsch, C. Numerical Computation of Internal and External Flows-Computational Methods for Inviscid and Viscous Flows, Vol. II, Wiley, 1990.

Kee, R.J., J.A. Miller and T.H. Jefferson, "Chemkin: A General-Purpose, Problem-Independent, Transportable, FORTRAN Chemical Kinetics Code Package." Sandia National Laboratories, SAND80-80003, Livermore, CA, 1980.

Kuo, K.K., *Principles of Combustion*, John Wiley and Sons, New York, 1986.

Ramadan, Khalid Mustafa. 2002. A computational study of pulsed detonation thermal spraying. PhD thesis, Department of Mechanical Engineering, The University of Iowa.

Ramadan, K., and P. B. Butler, "A Two-Dimensional Axisymmetric Flow Model for the Analysis of Pulsed Detonation Thermal Spraying," Combustion Science and Technology, Vol. 175, No. 9, 2003, pp. 1649-1677.

Saad, Michel A. 1993. *Compressible fluid flow.* 2nd ed. New Jersey: Prentice-Hall.

Schmitt, R.G., Department of Mechanical Engineering, "Analysis of Gas-Phase Detonation Wave Structure at Elevated Initial Pressures," (Ph.D.) 1994.

Schmitt, R.G., and Butler, P.B., "Detonation Properties of Gases at Elevated Initial Pressures," Combustion Science and Technology, Vol. 106, No. 1-3, 1995, pp. 167-193.

Schmitt, R.G., and Butler, P.B., "Detonation Wave Structure of Gases at Elevated Initial Pressures," Combustion Science and Technology, Vol. 107, No. 4-6, 1995, pp. 355-386.

Schmitt, R.G., Butler, P.B., and Freesmeier, J.J., "Performance and CO Production of a Non-Azide Airbag Propellant in a Pre-Pressurized Gas Generator," *Combustion Science and Technology*, Vol. 122, 1997, pp. 305-350.

Shu, C., Osher, S. Efficient Implementation of Essentially Non-oscillatory Shock-Capturing Schemes, Journal of Computational Physics, 1988, 77:439-471.

Steger, J.D., Warming, R.F. Flux Vector Splitting of the Inviscid Gasdynamic equations With Applications to Finite-Difference Methods, Journal of Computational Physics, 1981, 40; 263-293.

Toro, E.F., Riemann Solvers and Numerical Methods for Fluid Dynamics, 2nd Edition, Springer, 1999

Zucrow, M.J., and J.D. Hoffman, *Gas Dynamics*, Vol. 1, John Wiley and Sons, New York, 1976.